

INTERPLAY OF GEOMETRY WITH IMPURITIES AND DEFECTS IN TOPOLOGICAL STATES OF MATTER

by

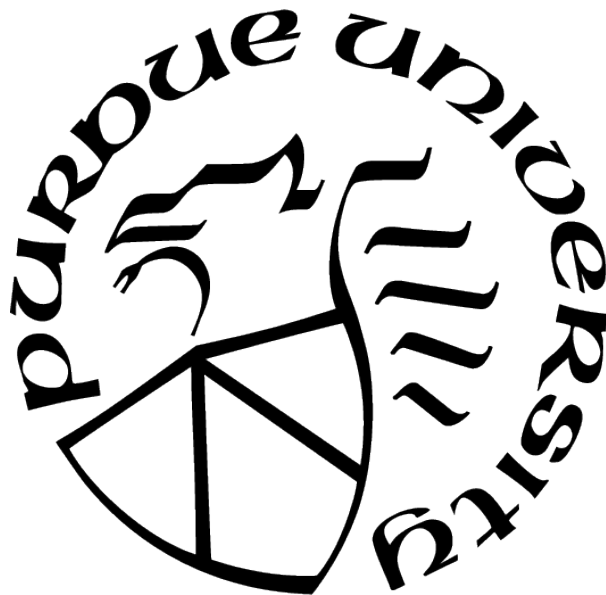
Guodong Jiang

A Dissertation

Submitted to the Faculty of Purdue University

In Partial Fulfillment of the Requirements for the degree of

Doctor of Philosophy



Department of Physics and Astronomy

West Lafayette, Indiana

May 2021

**THE PURDUE UNIVERSITY GRADUATE SCHOOL
STATEMENT OF COMMITTEE APPROVAL**

Dr. Rudro Biswas, Chair

Department of Physics and Astronomy

Dr. Gabor Csathy

Department of Physics and Astronomy

Dr. Chris Greene

Department of Physics and Astronomy

Dr. Michael Manfra

Department of Physics and Astronomy

Approved by:

Dr. John Finley

To my girlfriend, Angie Liu

ACKNOWLEDGMENTS

Throughout the writing of this thesis I have received a great deal of support and assistance from all directions.

I would like to thank my supervisor Dr. Rudro Biswas first for his invaluable expertise in formulating the research problems and insightful feedback to push me forward to finish the projects.

I would like to thank my collaborator Dr. Yang Xu for his genius design of experiments and fruitful discussions over three-dimensional topological insulators.

I want to thank my friend Dr. Wenzhe Yang for his patient advice and enlightening discussions on lattice systems in solid state physics.

In addition, I want to thank my colleagues Yingkang Chen, Rishabh Khare and Dewan Woods for their valuable guidance and discussions, which always pointed me to the right direction in research.

Finally, I would like to thank my girlfriend, Angie Liu, and my families for their strong and forever love, which encouraged me to overcome all kinds of obstacles in the seven years.

TABLE OF CONTENTS

LIST OF TABLES	7
LIST OF FIGURES	8
ABSTRACT	9
1 TOPOLOGICAL INSULATING QUANTUM STATES OF MATTER	10
1.1 Introduction	10
1.2 Boundary States from Dirac Equations	13
1.3 Boundary States from Modified Dirac Equations	17
1.4 Topological Invariants Of Bulk Hamiltonian	21
1.5 Summary	27
2 CONNECTION TOPOLOGY OF STEP EDGE BANDS AT THE SURFACE OF 3D TOPOLOGICAL INSULATORS	29
2.1 Introduction	29
2.2 Topological Insulator Surface States Perturbed by a Line Defect	29
2.3 In Presence of Perpendicular Magnetic Field	33
2.4 Summary	34
2.5 Chapter Acknowledgements	35
3 3D TOPOLOGICAL INSULATOR THIN FILMS WITH PARALLEL MAGNETIC FIELD	36
3.1 Introduction	36
3.2 Hybridization of Surfaces of TI Thin Films	37
3.3 Insulator-Semimetal Transition Driven By Parallel Magnetic Field	39
3.4 Summary	44
3.5 Chapter Acknowledgements	45
4 TOPOLOGICAL GRAVITATIONAL RESPONSE IN TWO-DIMENSIONAL TOPO- LOGICAL MATERIALS	46

4.1	Introduction	46
4.2	Tight-binding Calculation of Disclination Charge	47
4.2.1	The Haldane Model	48
4.2.2	The QWZ Model	51
4.2.3	The Kane-Mele Model	54
4.3	Topological Gravitational Response – finding the GCC	57
4.4	Summary	60
5	GEOMETRIC RESPONSE OF QUANTUM HALL STATES TO ELECTRIC FIELDS	61
5.1	Introduction	61
5.2	Gauge Invariant Variables in Quantum Hall Physics	62
5.3	Response to Nonuniform Electric Field: Analytical Result	64
5.4	Response to Nonuniform Electric Field: Numerical Result	69
5.5	Summary and Future Work	73
5.6	Chapter Acknowledgements	76
	REFERENCES	77
A	ANALYTICAL SOLUTION TO BOUNDARY STATES OF MODIFIED DIRAC EQUATIONS	83
A.1	One-Dimensional Space	83
A.2	Two-Dimensional Space	84
A.3	Three-Dimensional Space	86
B	GAUGE TRANSFORMATION TO JOIN THE DISCLINATION	88
B.1	Unitary Representation of the Rotation Symmetry	88
B.2	Join the Boundary	88
C	A PERIODIC DEFINITION OF THE DISCLINATION HAMILTONIAN	91

LIST OF TABLES

4.1	Excess charge of Haldane Model, center-type disclination, $C = \pm 1$ phase.	51
4.2	Excess charge of Haldane Model, vertex-type disclination, $C = \pm 1$ phase.	51
4.3	Excess charge of QWZ model, center-type disclination, $C = 1$ phase.	53
4.4	Excess charge of QWZ model, center-type disclination, $C = -1$ phase.	54
4.5	Excess charge of QWZ model, vertex-type disclination, $C = 1$ phase.	54
4.6	Excess charge of QWZ model, vertex-type disclination, $C = -1$ phase.	54
4.7	Excess Charge of Kane-Mele Model, center-type disclination, QSH phase $0 < \phi < \pi$. 56	
4.8	Excess Charge of Kane-Mele model, vertex-type disclination, QSH phase $0 < \phi < \pi$. 57	

LIST OF FIGURES

1.1	Boundary state wavefunction and energy dispersion of Dirac model.	17
1.2	Boundary state wavefunction and energy dispersion of modified Dirac model. . .	22
1.3	Winding number in $d_x - d_z$ plane.	24
1.4	\mathbf{d} vector plot of a lattice Chern insulator model.	27
2.1	Bound state dispersion at line defect on surface of 3D TI without magnetic field, at different defect strength U	33
2.2	Bound state dispersion at line defect on surface of 3D TI in the presence of magnetic field, at different defect strength U	34
3.1	Conductivity measurement of BiSbTeSe ₂ thin films.	38
3.2	Insulating phase, $\Delta_0 > \varepsilon_B$	41
3.3	Critical semimetal phase, $\Delta_0 = \varepsilon_B$	42
3.4	Dirac-Weyl semimetal phase, $\Delta_0 < \varepsilon_B$	42
3.5	Magnetoresistance measurement of 3D TI thin films.	43
4.1	Phase diagram of Haldane model.	49
4.2	Center-type and vertex-type disclination of hexagonal lattice.	50
4.3	Cut-and-glue process to join a 5-sector center-type disclination of hexagonal lattice.	50
4.4	Center-type and vertex-type disclination of square lattice.	53
5.1	A geometric summary of how a non-uniform electric field, \mathbf{E} , deforms a cyclotron orbit.	67
5.2	Plot of the Hofstadter butterfly.	70
5.3	Disturbed Landau levels of Hofstadter model in the weak field limit.	71
5.4	The spatial variation of local fractional charge density modulation in a nonuniform (sinusoidal) electric field.	74
5.5	The spatial variation of local current density in a nonuniform (sinusoidal) electric field.	75
5.6	The variation of cyclotron orbit energy with orbit location.	76

ABSTRACT

The discovery of topological quantum states of matter has required physicists to look beyond Landau's theory of symmetry-breaking, previously the main paradigm for studying states of matter. This has led also to the development of new topological theories for describing the novel properties. In this dissertation an investigation in this frontier research area is presented, which looks at the interplay between the quantum geometry of these states, defects and disorder. After a brief introduction to the topological quantum states of matter considered herein, some aspects of my work in this area are described. First, the disorder-induced band structure engineering of topological insulator surface states is considered, which is possible due to their resilience from Anderson localization, and believed to be a consequence of their topological origin. Next, the idiosyncratic behavior of these same surface states is considered, as observed in experiments on thin film topological insulators, in response to competition between hybridization effects and an in-plane magnetic field. Then moving in a very different direction, the uncovering of topological 'gravitational' response is explained: the topologically-protected charge response of two dimensional gapped electronic topological states to a special kind of 0-dimensional boundary – a disclination – that encodes spatial curvature. Finally, an intriguing relation between the gravitational response of quantum Hall states, and their response to an apparently unrelated perturbation – nonuniform electric fields is reported.

1. TOPOLOGICAL INSULATING QUANTUM STATES OF MATTER

1.1 Introduction

Gapped electronic topological states of matter behave like insulators in their bulk but as conductors at their surfaces. Their band structures are characterized by gapless boundary states traversing the energy band gap in the bulk, where the boundary states refer to end states, edge states and surface states for 1,2,3-dimensional topological materials respectively. In this introductory chapter I will consider some paradigmatic models for demonstrating how such gapless surface modes arise and how the existence of these modes are related to bulk topological invariants.

The first electronic states that were identified as topological states of matter are the integer quantum Hall (IQH) states, which exhibit the integer quantum Hall effect (IQHE) [1]–[5]. A two dimensional electronic system placed in a perpendicular magnetic field, at low temperatures and strong magnetic fields, displays a staircase-like behavior in its Hall conductance (ratio of total current to the transverse voltage drop) when measured as a function of the magnetic field strength. Classically, this variation is expected to be a simple linear dependence on the inverse of the magnetic field strength. At these plateaus, with unanticipated precision, the values of Hall conductance are quantized at integer multiples of a combination of fundamental constants of nature, the conductance quantum $\sigma_0 = e^2/h$. The system, when parked at any of these integer-quantized plateaus, is said to exhibit the IQHE. For very good quality materials, this quantization can also occur at σ_0 times a rational fraction, when the material exhibits the fractional quantum Hall effect (FQHE) [6], [7]. The IQH states can arise in systems of non-interacting electrons, while the existence of fractional quantum Hall states (FQH) depends on the presence of electronic interactions.

The first theoretical understanding of the IQHE was given by Laughlin using a thought experiment [2]. In his thought experiment, the gapped two-dimensional electronic state is imagined to exist on the surface of a cylinder. A thin thread of magnetic flux passing along the axis of the cylinder is then turned on and slowly but steadily increased so as to induce an azimuthal electromotive force parallel the cylinder surface. If the increase of flux

is slow enough, the system evolves adiabatically, continuing to remain in its instantaneous ground state. Every time the magnetic flux increases by a flux quantum $\phi_0 = h/e$, the ground state wavefunction is repeated, i.e., the system ‘goes back to itself’. Thus, during this time period an integer number, ν , of electrons must have been transported across the cylinder along the axial direction. This transfer can be re-interpreted as arising from a different source: due to the integrated Hall current that arises in response to the induced azimuthal electric field. Comparing the two, Laughlin deduced that the Hall conductance of the gapped electronic state is $\sigma_H = \nu e^2/h$. Laughlin’s argument thus yielded a very general result: the Hall conductance of a gapped electronic system without fractional charges is an integer multiple of the conductance quantum; it thus either exhibits IQHE or a zero Hall conductance. Laughlin’s argument can be recast to show that this ‘quantization’ behavior arises from how the many-body wavefunction behaves as a function of phase twist boundary conditions in two orthogonal directions (which form a torus because both phase twists are periodic), thus leading to the characterization of this quantization as ‘topological’.

Laughlin’s argument successfully connected the quantization of Hall conductance in IQH states to the fundamental physics principles of gauge invariance and charge quantization. The topological nature of this quantization was firmly established when the integer ν (see above) in the Hall conductance was shown to be equal to the Chern number of the electronic band structure by Thouless et al [8]. The Chern number is an integer-valued topological invariant characterizing the occupied valence band, viewed as a functional mapping from the crystal momentum space – the Brillouin zone torus – to the Bloch wavefunction space.

Following the discovery of IQH states, various other types of topological materials have also been discovered or proposed. Like the IQH states, these electronic materials are called ‘topological’ because they are characterized by topological invariants peculiar to their internal quantum structure, such as how their Bloch wavefunctions are defined over the crystal momentum Brillouin zone. Significant examples of such topological electronic states include Chern insulators [9] and time-reversal invariant topological insulators [10]–[12]. Chern insulators have nonzero quantized Hall conductance in absence of a net external magnetic field, thus exhibiting the so-called quantum anomalous Hall effect (QAHE). Topological insulators, on the other hand, are electronic band insulators which respect time-reversal symmetry

(TRS) but have gapless surface states which traverse the bulk band gap. These gapless states are ‘protected’ by TRS – as long as the Hamiltonian respects time reversal and the bulk band gap does not close, one can continuously modify the Hamiltonian as one wishes, including by adding disorder, but will not be able to get rid of the gapless character of the surface states.

As mentioned at the very beginning of this chapter, a significant property of topological quantum states is the existence of gapless modes at the surface. It is widely believed, given the absence of examples to the contrary, that the bulk topological invariant is encoded in the properties of its boundary states. For instance, the Chern number of QHE or QAHE of a two dimensional gapped electronic system can be obtained either (i) from the bulk band structure [8], or (ii) from the net number of conducting chiral edge modes, i.e., the difference between the number of right and left-moving edge modes. This sort of functional relation between the bulk Hamiltonian and boundary states has been observed in all topological phases of matter and is called the ‘bulk-boundary correspondence’ [13], [14]. The study of bulk topological properties, encoded in the geometry of the bulk wavefunctions, thus goes hand in hand with studying some unusual properties of the topological boundary states.

Later in this dissertation I will consider multiple examples of such connections. In Chapter 2 I discuss disorder-induced band structure engineering of topological insulator surface states, which is possible due to their resilience from Anderson localization, believed to be a consequence of their topological roots. In Chapter 3 I investigate the peculiar behavior of these same surface states, as observed in experiments, in response to turning on a magnetic field, which breaks time reversal symmetry that protects the topological properties of the material. In Chapter 4 I uncover topological ‘gravitational’ response: the topologically-protected charge response of two dimensional gapped electronic topological states to a special kind of 0-dimensional boundary – a disclination – which encodes spatial curvature (hence the historical usage of ‘gravitation’ referring to spacetime curvature). Finally, in Chapter 5 I consider the intriguing relation between gravitational response and responses to an apparently unrelated perturbation: nonuniform electric fields.

During the rest of this chapter I will study some prototypical analytical models to demonstrate the emergence of gapless topological boundary modes and the related bulk topological invariants.

1.2 Boundary States from Dirac Equations

Many analytical models exist which demonstrate how bulk topological Hamiltonians give rise to gapless boundary states [15]–[18]. A general class of approaches start from the massive Dirac equation in the bulk, giving rise to the Jackiw-Rebbi surface modes which decay exponentially away from the boundary [19], [20]. I initially cover this approach below. Within this approach, one can conclude that Dirac modes with masses of opposite sign belong to distinct topological classes; however, one cannot identify the topologically ‘nontrivial’ phase within this approach [16], [21], [22]. Then I consider band structures satisfying the modified Dirac equation (MDE) with a quadratic mass term. This approach has the advantage of allowing one to unambiguously identify the topologically ‘trivial’ and ‘non-trivial’ phases within the same region of space. Topological conditions under which these equations lead to boundary state are derived, and the connection to topological invariants of the bulk Hamiltonian is explained.

The Dirac equation is a relativistic wave equation describing spin-1/2 particles [23]. It is relevant to the theory of topological states because the low-energy effective Hamiltonians for two and three-dimensional topological insulators have the same structure as the Dirac Hamiltonian in the corresponding dimension [10], [24], [25]. Therefore, the Dirac equation is a rich analytical playground for exploring low-energy topological boundary states and the physics of topological phase transitions [24]. The massive Dirac equation has the form

$$\hat{\mathcal{H}}\psi \equiv (cp_i\alpha_i + mc^2\beta)\psi = E\psi, \quad (1.1)$$

where m is the mass and c the speed of light. The $\{\alpha_i\}$, i going over the spatial dimensions, and β are known as Dirac matrices. They satisfy the Clifford algebra

$$\alpha_i^2 = \beta^2 = 1, \quad \{\alpha_i, \alpha_j\} = 0, \quad \{\alpha_i, \beta\} = 0. \quad (1.2)$$

Here $\{, \}$ denotes anti-commutation relation. These matrices can be used to generate representations of the Lorentz group, i.e., the group of boosts and rotations.

In 1+1 and 2+1 spacetime dimensions, the matrices $\{\alpha_i, \beta\}$ have to be at least 2-dimensional; in 3+1 dimensions, they have to be at least 4-dimensional [23]. Let's first take 1D space as an example to see how Dirac equation can lead to a bound state solution, and then generalize it to higher dimensions.

Consider the one-dimensional case where an interface between topological trivial and nontrivial phases is located at $x = 0$. We choose the following representation of the Dirac matrices in terms of the Pauli matrices: $\alpha = \sigma_x$, $\beta = \sigma_z$. Then the Dirac Hamiltonian becomes (setting $c = 1$ for now):

$$\hat{\mathcal{H}} = \sigma_x \hat{p}_x + \sigma_z m. \quad (1.3)$$

\hat{p}_x is the differential operator $-i\partial_x$. m is the mass which is equal to m_l in the left ($x < 0$) and m_r on the right ($x > 0$) [26], thus creating two different 'phases' in the two semi-infinite spaces. To find a bound state at the interface between these two phases, i.e., around $x = 0$, one uses the Jackiw-Rebbi ansatz [19]:

$$\psi(x) = e^{\mp \lambda_{\pm} x} \chi \text{ for } x \gtrless 0, \quad (1.4)$$

where χ is a 2-dimensional spinor and the existence of real positive λ_{\pm} are to be determined by solving the wave equation. Plugging this form into Equation (1.3) one obtains an eigenvalue equation, from which λ_{\pm} can be written in terms of energy E . Imposing continuity of wavefunction at $x = 0$, one arrives at the following condition:

$$\frac{\sqrt{m_l^2 - E^2}}{m_l - E} = -\frac{\sqrt{m_r^2 - E^2}}{m_r - E}. \quad (1.5)$$

Equation (1.5) determines the energy spectrum of possible boundary modes. One finds that this energy is unique, $E = 0$, and in order to have this mode the masses on two sides must be of opposite sign,

$$\text{sgn}(m_l m_r) = -1. \quad (1.6)$$

Thus, there is a qualitative (topological, see below) difference between two gapped Dirac fermion phases only when their masses have opposite sign and this is captured in the existence of a zero energy mode at their interface. This result can be generalized to any continuous variation of $m(x)$ across the interface, as long as it asymptotically tends to $m_{l,r}$ on the left/right.

This Jackiw-Rebbi bound mode at the interface of topologically inequivalent phases of the Dirac model can be straightforwardly generalized to higher dimensions. In 2+1 dimensions, consider a line interface located at $x = 0$. One can choose $\alpha_1 = \sigma_x$, $\alpha_2 = \sigma_y$ and $\beta = \sigma_z$ as a representation of Clifford algebra, leading to the Dirac Hamiltonian:

$$\hat{\mathcal{H}}_+ = \sigma_x \hat{p}_x + \sigma_y \hat{p}_y + \sigma_z m. \quad (1.7)$$

The subscript $+$ indicates the ‘helicity’ of Dirac fermion. The helicity is the eigenvalue of the helicity operator: the projection of spin in the direction of momentum, $(1/2)\boldsymbol{\sigma} \cdot \mathbf{p}/|\mathbf{p}|$. Since the system has translational symmetry along y direction, one can use the following ansatz for edge state wavefunctions bound at interface: $\psi(x, y) = e^{ik_y y} e^{\lambda x} \chi$, where k_y is the quantum number labeling momentum along y direction. Similar to the 1+1-dimensional problem, continuity of the wavefunction at $x = 0$ leads to a consistency condition followed by the conclusion that the masses on the two sides of the interface must satisfy condition (1.6) in order for the edge mode to exist. Unlike in the 1+1-dimensional case, it is found that the edge mode energy has a *gapless* linear dispersion:

$$E = k_y \text{sgn}(m_r). \quad (1.8)$$

The Hamiltonian $\hat{\mathcal{H}}_+$ is not time-reversal invariant. Defining the time-reversal operator as $\hat{T} = i\sigma_y K$, where K is complex conjugation, the time-reversal counterpart of $\hat{\mathcal{H}}_+$ is a Dirac Hamiltonian with opposite helicity:

$$\hat{\mathcal{H}}_- = \hat{T}\hat{\mathcal{H}}_+\hat{T}^{-1} = \sigma_x\hat{p}_x - \sigma_y\hat{p}_y + \sigma_z m. \quad (1.9)$$

Similar to $\hat{\mathcal{H}}_+$, when condition (1.6) is satisfied across the interface, gapless edge modes exist and dispersion is

$$E = -k_y \text{sgn}(m_r). \quad (1.10)$$

Here the group velocity changes sign because k_y maps to $-k_y$ under time reversal symmetry. Equations (1.8) and (1.10) are dispersions corresponding to the so-called helical/chiral edge modes of the Dirac equation in 2+1 dimensions.

In 3+1 dimensions, the minimum dimension for a representation of the Clifford algebra is four. Such a representation is given in terms of the Pauli matrices thus: $\alpha_i = s_x \otimes \sigma_i$ and $\beta = s_z \otimes \sigma_0$. The Dirac Hamiltonian is:

$$\hat{\mathcal{H}} = \alpha_x\hat{p}_x + \alpha_y\hat{p}_y + \alpha_z\hat{p}_z + \beta m. \quad (1.11)$$

Considering two gapped phases with masses m_l, m_r separated by an interface at $x = 0$, one assumes the ansatz wavefunctions $\psi(x, y, z) = e^{i(k_y y + k_z z)} e^{\lambda x} \chi$, where k_y, k_z label the momentum in $y-z$ plane. Solving the eigenvalue equations one can find two surface modes with dispersions $E_{\pm} = \pm \sqrt{k^2 + m^2 - \lambda_{l,r}^2}$, where $k^2 = k_x^2 + k_y^2$ and $\lambda_{l,r}$ are yet to be determined, indicating the exponential localizations of the surface modes in the two phases. Before considering the continuity condition across the interface, at a specific bound state energy E , on each side of the interface there are two independent allowed eigenvectors χ_1, χ_2 . Therefore, a general surface state wavefunction is a linear combination of the two spinors, with coefficients a_l, b_l, a_r, b_r . Imposing continuity of the wavefunction at the interface, i.e., using an equation

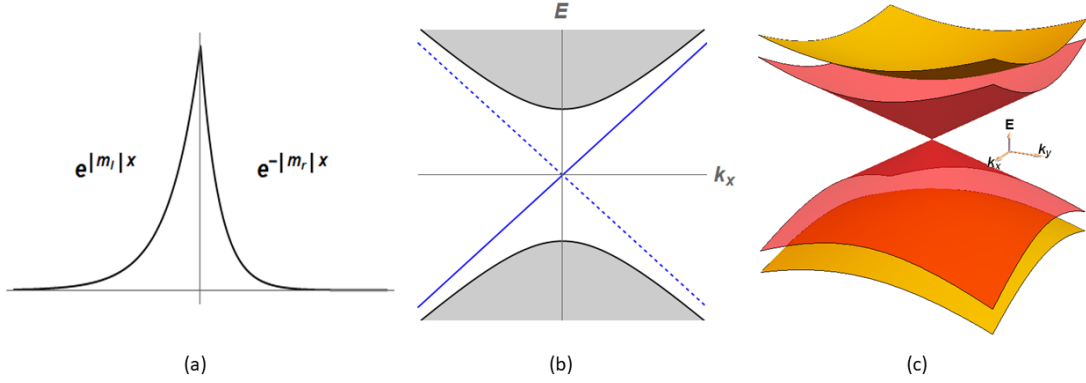


Figure 1.1. Boundary state wavefunction and energy dispersion of Dirac model. (a) Wavefunction profile along x direction of a boundary state at interface. (b) Energy spectrum of 2D Dirac model, bulk bands in grey and linearly dispersed helical edge modes in blue. Dashed blue line shows dispersion of edge modes in the time-reversal counterpart. (c) Energy spectrum of 3D Dirac model, top and bottom of bulk bands in yellow and doubly degenerate surface bands in red.

of the form $a_l\chi_{l1} + b_l\chi_{l2} = a_r\chi_{r1} + b_r\chi_{r2}$, one again arrives at condition (1.6) for the surface states to exist. These surface states have a 2+1-dimensional *gapless* Dirac dispersion:

$$E = \pm k = \pm \sqrt{k_x^2 + k_y^2}. \quad (1.12)$$

So far I have reviewed the main features of gapless interface modes at the junction of topologically inequivalent Dirac fermions in one, two and three spatial dimensions. Their energy spectra correspond to an isolated zero mode, a linear-dispersing helical edge mode and a 2+1-dimensional Dirac-like dispersion, respectively (Figure 1.1). Such boundary mode dispersions have been widely observed in experiments and numerics [11], [25]. The Dirac Hamiltonian thus serves as a crude effective long wavelength model encapsulating the physics of topological band insulators.

1.3 Boundary States from Modified Dirac Equations

In the preceding calculations one has seen that the existence of boundary states at the interface between two Dirac band structures requires the Dirac masses on the two sides to

have opposite signs. This does not let one consider the absolute topological non-triviality of either phase with respect to vacuum which is, as tacitly assumed, topologically trivial. I describe now a modified Dirac model for boundary states which allows one to compare the topological nature of the Dirac phase vs. vacuum [20], [22].

Starting from the 1+1-dimensional case, I will consider how the Dirac equation dressed with a quadratic mass term, the so-called modified Dirac equation (MDE), possesses boundary states when satisfying a topological condition which depends only on parameter values of the MDE phase; placing another Dirac fermion on the other side of the interface is no longer needed. This allows one to consider a topologically trivial vacuum on the other side, and thus vanishing of the wavefunction there. I will extend this method to higher spatial dimensions. In particular, I obtain the exact boundary state solutions to the MDE in two- and three-dimensional space, instead of using a perturbation method [20], [22]. More details of analytical solutions to MDEs are provided in Appendix A.

In 1+1 dimensions, the modified Dirac Hamiltonian is

$$\hat{\mathcal{H}} = \sigma_x \hat{p}_x + \sigma_z (m - B \hat{p}_x^2). \quad (1.13)$$

Comparing with the Dirac equation (1.3), the mass term has been modified with a quadratic contribution, $-B \hat{p}_x^2$. This correction can be motivated as arising from retaining more terms in the Taylor expansion of the band Hamiltonian near the Dirac point momentum. Suppose now that the region $x > 0$ is topological and bound states are localized near $x = 0$. Similar to the Dirac equation, one can assume an ansatz solution of the form $\psi(x) = e^{\lambda x} \chi$ for $x > 0$, while the wavefunction vanishes for $x \leq 0$. The Schrödinger equation, $\hat{\mathcal{H}}\psi = E\psi$, leads to the following quartic equation for λ :

$$E^2 = (m + B\lambda^2)^2 - \lambda^2. \quad (1.14)$$

The four roots of this equation come in pairs, which are denoted by $\pm\lambda_1, \pm\lambda_2$. One finds that

$$\lambda_{1,2}^2 = \frac{1}{2B^2} \left(1 - 2mB \pm \sqrt{1 + 4B^2E^2 - 4mB} \right). \quad (1.15)$$

Localization of the boundary states to the region near $x = 0$ requires these roots to have negative real parts – this will be referred to as the ‘decaying condition’ below. Imposing the boundary condition at the interface, $\psi(0) = 0$, one needs to find two distinct roots with negative real parts, $\lambda_{1,2}$, which possess a common spinor as the allowed eigenvector. The boundary mode can then be constructed as

$$\psi(x) = (e^{\lambda_1 x} - e^{\lambda_2 x})\chi. \quad (1.16)$$

Inspecting Equation (1.15), the decaying condition is satisfied if

$$\begin{aligned} 1 + 4B^2E^2 - 4mB &< 0, \\ \text{or, } 1 + 4B^2E^2 - 4mB &> 0 \text{ and } mB < \frac{1}{2} \text{ and } E^2 < m^2. \end{aligned} \quad (1.17)$$

After some algebra, from the vanishing of wavefunction at $x = 0$, i.e. $\chi_1 = \chi_2$, it is found that the only possible solution to boundary state energy is $E = 0$. To have this solution, a topological condition must be satisfied,

$$mB > 0. \quad (1.18)$$

This is a simple condition expressed in terms of parameters of the given bulk Hamiltonian (1.13) only, no longer relying on comparing with another Dirac phase across the interface.

Next, consider the MDE in 2+1 dimensions. Suppose there is a line interface at $x = 0$ and $x > 0$ is the topological region to be investigated. As usual, $\psi(0) = 0$, the condition for there being a vacuum on the other side. The Hamiltonian with positive helicity is:

$$\hat{\mathcal{H}}_+ = \sigma_x \hat{p}_x + \sigma_y \hat{p}_y + \sigma_z (m - B\hat{p}^2), \quad (1.19)$$

where $\hat{p}^2 = \hat{p}_x^2 + \hat{p}_y^2$. To find edge modes localized at $x = 0$, one assumes the ansatz $\psi(x, y) = e^{ik_y y} e^{\lambda x} \chi$ and the Schrodinger equation leads to a quartic equation for λ :

$$E^2 = (m - Bk_y^2 + B\lambda^2)^2 + k_y^2 - \lambda^2. \quad (1.20)$$

The four roots are $\pm\lambda_1$ and $\pm\lambda_2$, with

$$\lambda_{1,2}^2 = \frac{1}{2B^2} (1 - 2mB + 2B^2 k_y^2 \pm \sqrt{1 + 4B^2 E^2 - 4mB}). \quad (1.21)$$

Similar to the 1+1-dimensional problem analysis, existence of two roots with negative real parts necessitate the following condition:

$$\begin{aligned} 1 + 4B^2 E^2 - 4mB &< 0, \\ \text{or, } 1 + 4B^2 E^2 - 4mB &> 0 \text{ and } mB < \frac{1}{2} + B^2 k_y^2 \\ \text{and } E^2 &< k_y^2 + (m - Bk_y^2)^2. \end{aligned} \quad (1.22)$$

Imposing now the boundary condition $\psi(0) = 0$, one finds a linear energy spectrum at the boundary:

$$E = \text{sgn}(B)k_y. \quad (1.23)$$

Meanwhile, the vanishing of wavefunction at interface reproduces the same topological condition (1.18) as the 1+1 dimensional MDE.

For the time-reversed MDE counterpart, $\hat{\mathcal{H}}_- = \sigma_x \hat{p}_x - \sigma_y \hat{p}_y + \sigma_z (m - B\hat{p}^2)$, we find the same topological condition but an inverted linear dispersion, $E = -\text{sgn}(B)k_y$. The edge modes of $\hat{\mathcal{H}}_{\pm}$, corresponding to the momentum $\pm k_y$, have equal energy but opposite group velocity, and are thus referred to as helical/chiral modes.

Finally, in 3+1 dimensions, one can choose the Clifford algebra representation same as Dirac equation, $\alpha_i = s_x \otimes \sigma_i$ and $\beta = s_z \otimes \sigma_0$, with $i = x, y, z$. The MDE Hamiltonian is

$$\hat{\mathcal{H}} = \alpha_x \hat{p}_x + \alpha_y \hat{p}_y + \alpha_z \hat{p}_z + \beta (m - B\hat{p}^2). \quad (1.24)$$

Here $\hat{p}^2 = \hat{p}_x^2 + \hat{p}_y^2 + \hat{p}_z^2$. Assuming the surface mode ansatz $\psi(x, y, z) = e^{i(k_y y + k_z z)} e^{\lambda x} \chi$ for $x > 0$, the Schrödinger equation leads to the following quartic equation for λ :

$$E^2 = (m - Bk^2 + B\lambda^2)^2 + k^2 - \lambda^2, \quad (1.25)$$

with $k^2 = k_x^2 + k_y^2$. The four roots are $\pm\lambda_1$ and $\pm\lambda_2$, with

$$\lambda_{1,2}^2 = \frac{1}{2B^2} (1 - 2mB + 2B^2 k_y^2 + 2B^2 k_z^2 \pm \sqrt{1 + 4B^2 E^2 - 4mB}). \quad (1.26)$$

Similar to the lower dimensional cases, a decaying condition needs to be satisfied, leading to a similar set of conditions. Incorporating the boundary condition at interface, $\psi(0) = 0$, one obtains the following energy dispersion of the surface states:

$$E = \pm k = \pm \sqrt{k_x^2 + k_y^2}. \quad (1.27)$$

This is a Dirac-cone dispersion relation which is same as that obtained from Dirac equation in three-dimensional space. One also finds the same topological condition $mB > 0$ as before.

We note, in closing, that the boundary modes for all three cases of MDEs studied have the same energy spectrum as a *gapless* Dirac fermion in one lower spatial dimension. Also note that these boundary mode dispersions are restricted to the energy range $|E| < \sqrt{m/B}$, at which energy the interface bands merge with the bulk bands. The wavefunction profile and dispersion relations of modified Dirac models are illustrated in Figure 1.2.

In the next section I connect the topological criterion for obtaining boundary states with bulk topological invariants for the MDE.

1.4 Topological Invariants Of Bulk Hamiltonian

This section reviews the theory of the topological invariant corresponding to a two-band Chern insulator [9], [21]. I apply this criterion to the MDE and show that the topological condition is the same as obtained when considering the existence of gapless surface states .

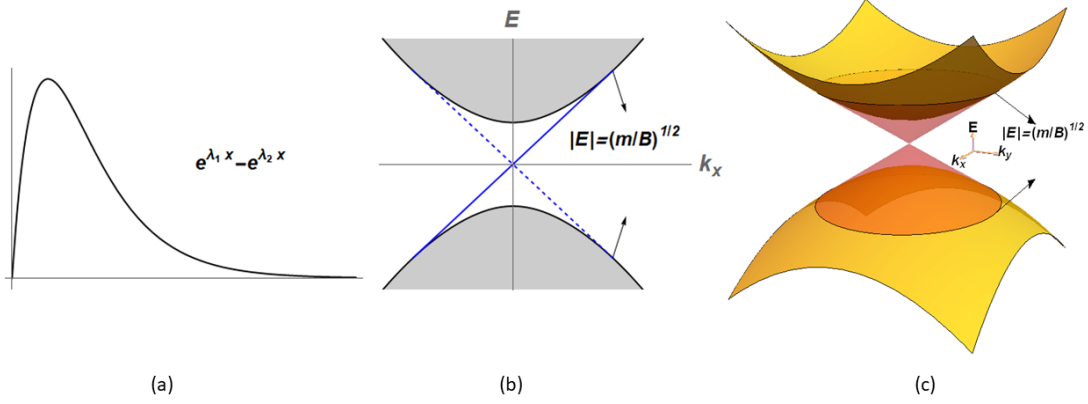


Figure 1.2. Boundary state wavefunction and energy dispersion of modified Dirac model. (a) Wavefunction profile along x direction of a boundary state on one side of the interface, where $\lambda_{1,2}$ are roots with negative real part solved from the polynomial equation. To generate this plot both $\lambda_{1,2}$ being real and negative are assumed. (b) Energy spectrum of 2D modified Dirac model, bulk bands in grey and linearly dispersed helical edge modes in blue. Dashed blue line shows dispersion of edge modes in the time-reversal counterpart. (c) Energy spectrum of 3D modified Dirac model, top and bottom of bulk bands in yellow and doubly degenerate surface bands in red. For (b) and (c), $|E| = \sqrt{m/B}$ is the cutoff energy of edge/surface state band where it intercepts with bulk bands.

Consider a generic two-band lattice model. The Hamiltonian in momentum space can be expressed using Pauli matrices:

$$h(\mathbf{k}) = d_0(\mathbf{k}) + \sum_{i=x,y,z} d_i(\mathbf{k})\sigma_i. \quad (1.28)$$

\mathbf{k} is the crystal momentum and $d_0, \{d_i\}$ are all real functions. Since the crystal momentum space is periodic across the Brillouin zone due the Bloch's theorem, the space of \mathbf{k} is homeomorphic to the circle (S), torus ($S \times S$) and three-torus ($S \times S \times S$) in one, two and three spatial dimensions respectively. The energy spectrum of this two-band model is

$$\varepsilon_{\pm}(\mathbf{k}) = d_0(\mathbf{k}) \pm d(\mathbf{k}), \quad (1.29)$$

where $d = \sqrt{d_x^2 + d_y^2 + d_z^2}$ is the magnitude of $\mathbf{d} \equiv (d_x, d_y, d_z)$. d_0 controls the zero point of energy at each momentum \mathbf{k} and vector \mathbf{d} determines the band gap at that momentum. With functions d_x, d_y, d_z , the space of crystal momentum \mathbf{k} is mapped to a closed manifold in \mathbf{d} -space. Since considering insulators only, the band gap never closes and one has to exclude the origin when considering \mathbf{d} -space, which makes this space homotopy-equivalent to a 2-sphere.

Using this formulation, one can now find all possible classes of 2-band insulating Hamiltonians which cannot be transformed continuously into each other without closing the energy gap. This is just equal to the number of ways that the Brillouin zone can be mapped to the 2-sphere corresponding to \mathbf{d} -space without the origin.

For example, consider the one-dimensional case first. Crystal momentum has only one component k_x , so under function d_x, d_y, d_z , the k_x -circle is mapped to a loop in \mathbf{d} -space, the 2-sphere. Since all loops on a sphere surface can be shrunk to a single point by continuous deformation, there is only one ‘trivial’ class of such Hamiltonians.

But then, how to obtain a ‘nontrivial’ phase of the MDE? To see how that came about, consider the Hamiltonian to be constrained by symmetries [27]. Suppose that the Hamiltonian has a chiral symmetry $\hat{\Gamma} = \sigma_y$:

$$\hat{\Gamma}\hat{\mathcal{H}}\hat{\Gamma} = -\hat{\mathcal{H}}, \quad (1.30)$$

such that under this chiral symmetry an energy eigenstate is transformed to another state of opposite energy. Plugging in the Hamiltonian (1.28), one finds that $d_0 = 0$ and more importantly, $d_y = 0$ also. Thus, under this symmetry, \mathbf{d} -space minus the origin is equivalent to a 1-sphere, i.e., a circle.

Since a circle mapping to another circle can be characterized by the winding number, an integer, therefore there exists an infinity of topologically distinct classes of chiral 2-band Hamiltonians in 1+1 dimensions. Each topological class is labeled by an integer-valued winding number and Hamiltonians cannot be continuously transformed between distinct

topological classes without closing the energy gap (see Figure 1.3). This is a primitive example of a symmetry-protected topological (SPT) insulator.

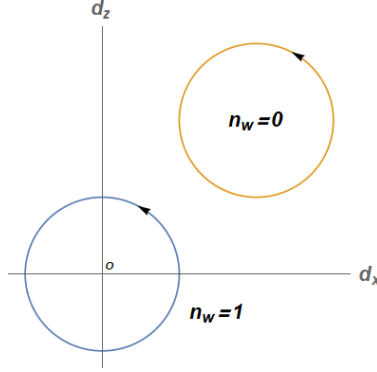


Figure 1.3. Winding number in $d_x - d_z$ plane. Two loops with winding number +1 (blue) and 0 (yellow) are shown. Black arrows show direction of increasing parameter k_x . To deform one loop to the other, it must pass the origin of $d_x - d_z$ plane (gap closing) or be lifted away from the plane (breaking chiral symmetry), crossing d_y axis and back to the plane again.

The winding number can be analytically calculated thus. Introduce a complex function $\alpha = d_x + id_z$. The winding number is then the number of times α winds around the origin in the complex plane as k_x traverses the Brillouin zone once:

$$n_w = \frac{1}{2\pi i} \oint_{\gamma} \frac{d\alpha}{\alpha}, \quad (1.31)$$

where γ is the mapping loop of momentum k_x . If the one-dimensional Brillouin zone is chosen to be $[0, 2\pi]$, this integral can be converted to

$$n_w = \frac{1}{2\pi i} \int_0^{2\pi} \frac{d'_x + id'_z}{d_x + id_z} dk_x. \quad (1.32)$$

The winding number is a topological invariant, and topological phases of distinct winding numbers cannot be continuously deformed into one another. Mathematically, this is because integers are discrete so there is no way to change from one to another continuously. Alternately, physically, if one wants to continuously modify a loop (representing a starting Hamiltonian) to the other with a different winding number (the final Hamiltonian in a dif-

ferent class), it must pass the origin, which means that the energy gap will need to close sometime(s) during the process. Otherwise, one can lift the loop off $d_x - d_z$ plane, passing through d_y axis and then back to the plane, which means breaking the chiral symmetry.

One can now apply formula (1.32) to the 1+1-dimensional MDE, where $d_x = p_x$, $d_z = m - Bp_x^2$ [20]. Assuming that the topological properties flow from the physics of the long wavelength effective Dirac model only, one can convert the integral limit in Equation (1.32) to $(-\infty, \infty)$. The replacement can be motivated by noting that in the continuum limit, the lattice constant approaches zero and thus the size of the Brillouin zone tends to infinity. Then the winding number of the 1+1-dimensional MDE is

$$n_w = \frac{1}{2\pi i} \int_{-\infty}^{\infty} \frac{1 - 2Bip_x}{p_x + i(m - Bp_x^2)} dp_x. \quad (1.33)$$

The quadratic correction term Bp_x^2 helps converge the integral. Using straightforward complex analysis, one finds that the winding number is equal to $-(1/2)[\text{sgn}(m) + \text{sgn}(B)]$, which means the phase is topological only when m and B have same sign. This is the same condition as the one required for observing the topological boundary mode in the MDE! Thus, I have shown that the boundary modes of the MDE are deeply related to a topological invariant of the bulk Hamiltonian. This reveals what is known as the bulk-boundary correspondence.

Next, consider the two-band insulator model in 2+1 dimensions. The two-dimensional Brillouin zone, $S \times S$, a 2-torus, now needs to be mapped to the 2-sphere-equivalent manifold in \mathbf{d} -space. Such maps are classified by the first Chern class or simply, the Chern number. The Chern number of valence band can be computed as [8]

$$C = \frac{i}{2\pi} \int_0^{2\pi} dk_x \int_0^{2\pi} dk_y \left(\left\langle \frac{\partial u_0}{\partial k_x} \middle| \frac{\partial u_0}{\partial k_y} \right\rangle - \left\langle \frac{\partial u_0}{\partial k_y} \middle| \frac{\partial u_0}{\partial k_x} \right\rangle \right), \quad (1.34)$$

where the Brillouin zone is assumed to be $[0, 2\pi] \times [0, 2\pi]$ and u_0 is the periodic part of valence band wavefunction. The quantity $i(\langle \partial u_0 / \partial k_x | \partial u_0 / \partial k_y \rangle - \langle \partial u_0 / \partial k_y | \partial u_0 / \partial k_x \rangle)$ is the ‘Berry curvature’ which measures the mismatch of Berry phases when transporting the function u_0 along different curves [28].

At first sight, the surface integral in (1.34) seems to always be zero (trivial), since if one introduces Berry connection $\mathbf{A} = i\langle u_0 | \nabla_{\mathbf{k}} u_0 \rangle$, the integral can be converted to a line integral of \mathbf{A} around the Brillouin zone boundary. Since the Brillouin zone boundary is equivalent to a point, this line integral is zero. This argument fails if the Berry curvature is not analytical everywhere on the Brillouin zone [29], which leads to the nontrivial case. In this case, the wavefunction is not single-valued on the torus of Brillouin zone. By a gauge fixing, one can show the Chern number is an integer which is the sum of winding numbers of these fixing gauges at all singular points in the Brillouin zone.

For the two-band insulator Hamiltonian (1.28), the Chern number of the valence band has a simple formula. Equation (1.34) can be rewritten as [30]

$$C = \frac{i}{2\pi} \int_0^{2\pi} dk_x \int_0^{2\pi} dk_y \text{tr}(\nabla_{\mathbf{k}} P \times P \nabla_{\mathbf{k}} P)_z, \quad (1.35)$$

where $\hat{P} = |u_0\rangle\langle u_0|$ is the projection operator onto the valence band. For the generic Hamiltonian (1.28), one finds that

$$\hat{P} = \frac{1}{2} \left(\mathbb{I} - \frac{\mathbf{d} \cdot \boldsymbol{\sigma}}{d} \right), \quad (1.36)$$

where \mathbb{I} is the 2 by 2 identity matrix. Using this in Equation (1.35), one obtains [21]

$$C = \frac{1}{4\pi} \int_0^{2\pi} dk_x \int_0^{2\pi} dk_y \frac{\mathbf{d} \cdot (\partial_{k_x} \mathbf{d} \times \partial_{k_y} \mathbf{d})}{d^3}. \quad (1.37)$$

Formula (1.37) allows one to calculate the Chern number from the \mathbf{d} vector of a two-band model Hamiltonian. It shows the Chern number is determined from how the 2-manifold parameterized by k_x, k_y encloses the topological defect $\mathbf{d} = 0$ [31]. Figure 1.4 shows the \mathbf{d} vector plot of a lattice Chern insulator model.

Let's now calculate the Chern number for the 2+1 dimensional MDE [22], where $d_x = p_x$, $d_y = p_y$ and $d_z = m - Bp^2$. In the continuum approximation, one can ignore the periodicity of p_x, p_y and replace the integral limits with $(-\infty, \infty)$. The Chern number of modified Dirac model is then

$$C = \frac{1}{4\pi} \int_{-\infty}^{\infty} dk_x \int_{-\infty}^{\infty} dk_y \frac{m + B(p_x^2 + p_y^2)}{\{p_x^2 + p_y^2 + [m - B(p_x^2 + p_y^2)]^2\}^{3/2}} = \frac{1}{2} [\text{sgn}(m) + \text{sgn}(B)]. \quad (1.38)$$

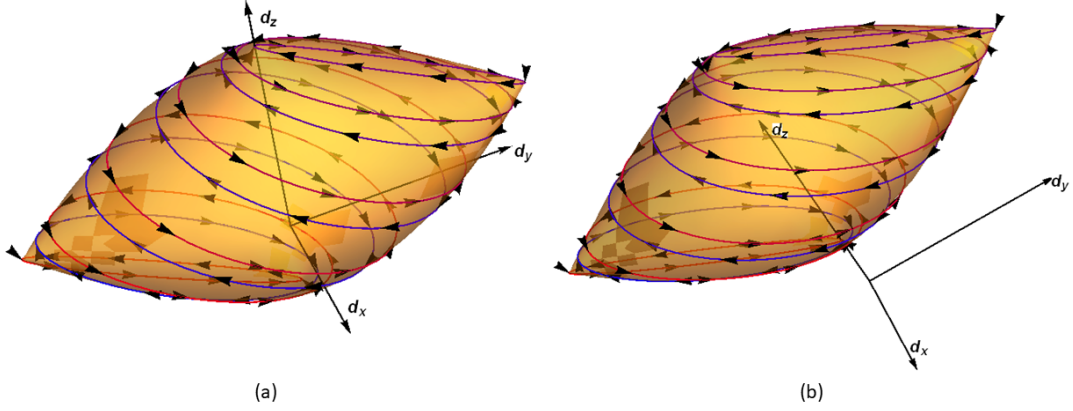


Figure 1.4. \mathbf{d} vector plot of a lattice Chern insulator model. This model has $d_x = -\sqrt{3}\sin k_x \sin k_y$, $d_y = \sqrt{3}(\cos k_x - \cos k_y)$ and $d_z = m - \cos k_x - \cos k_y$. The phase is nontrivial when $|m| < 2$ and trivial when $|m| > 2$. Each arrow loop shows the trace of \mathbf{d} vector as k_x goes from 0 to 2π at constant k_y . Color of loop changing from red to purple shows k_y going from 0 to 2π . (a) $m = 1$. The manifold wraps around the origin twice, and for the second wrap both $\partial_{k_x}\mathbf{d}$ and $\partial_{k_y}\mathbf{d}$ change direction so give equal contribution as first wrap, leading to $C = 2$. (b) $m = 3$. The manifold does not enclose origin. Each of the two wraps give zero Chern number so $C = 0$.

Similar to the 1+1 dimensional case, the phase of 2+1 dimensional MDE has a nonzero Chern number only when m and B have the same sign, agreeing with the previously obtained topological condition for the existence of gapless edge modes. For the time-reversal counterpart $\hat{\mathcal{H}}_-$, there is an additional minus sign in Chern number due to change of sign in $\mathbf{d} \cdot (\partial_{k_x}\mathbf{d} \times \partial_{k_y}\mathbf{d})$.

1.5 Summary

In this chapter I took a broad overview of electronic quantum topological band insulators. I modeled the topological materials using both simple and modified massive Dirac models. I motivated the winding number and Chern number as topological invariants and demonstrated the bulk-boundary correspondence by showing that the same topological index, which indicates nontrivial topology in the bulk, also indicates the presence of gapless

modes at the boundary. In what follows, I will delve deeper into some idiosyncratic properties that characterize these topological materials.

2. CONNECTION TOPOLOGY OF STEP EDGE BANDS AT THE SURFACE OF 3D TOPOLOGICAL INSULATORS

2.1 Introduction

Three-dimensional time reversal invariant topological insulators are materials characterized by a \mathbb{Z}_2 (yes/no) topological index [25], [32]–[35]. They have gapless two-dimensional surface states effectively described by an odd number of (2+1)-dimensional massless helical Dirac modes, whose gapless nature is protected by time reversal symmetry, even against disorder [25], [36]. Recent studies have shown that in such 3D topological insulators, step-like surface defects can introduce new in-gap states which modify the band structure near the Dirac point [37], [38]. These emergent in-gap states are one-dimensional – in experiments, they are observed to be localized along the step edge [39], [40].

In the remainder of the chapter, I will investigate the response of the topological insulator surface Dirac states to one-dimensional line defect, using the analytical non-perturbative T-matrix method [41]. I will show that one-dimensional bound modes appear at these defects and persist over a wide range of defect strengths. Moreover, near small momentum, such a bound one dimensional mode is linearly dispersing and the linear dispersion is always connected to the Dirac point of the surface states. This connectivity is destroyed by adding a magnetic field, which breaks time reversal symmetry. My continuum analytical results have also been confirmed by complimentary numerical calculations in [41].

2.2 Topological Insulator Surface States Perturbed by a Line Defect

In the last chapter we saw how the massive Dirac fermions in 3+1 dimensions give rise to massless 2+1 dimensional Dirac modes on the surface. To model these surface bands in the long wavelength limit, one can use the 2D massless Dirac Hamiltonian as a low-energy approximation to the band structure. In the long wavelength limit, one can model a general line defect on 3D topological insulator surface as a sharp delta function potential.

Incorporating such a defect at $x = 0$ and extending along the y direction, the surface Hamiltonian becomes

$$\hat{\mathcal{H}} = \hat{\mathcal{H}}_0 + \hat{V}, \quad \text{with } \hat{\mathcal{H}}_0 = \sigma_x \hat{p}_x + \sigma_y \hat{p}_y \quad \text{and} \quad \hat{V} = U\delta(\hat{x}). \quad (2.1)$$

Here, \hbar and Fermi velocity v_F have been set to 1. U characterizes the renormalized strength of the defect in the long length scale limit. It can be used as an effective fitting parameter to experimental/numerical results.

The unperturbed Hamiltonian, $\hat{\mathcal{H}}_0$, has the following energy eigenstates [42]:

$$\psi_{\mathbf{k},\pm}(\mathbf{r}) = \frac{1}{\sqrt{2L_x L_y}} e^{i\mathbf{k}\cdot\mathbf{r}} \begin{pmatrix} e^{-i\phi_{\mathbf{k}}} \\ \pm 1 \end{pmatrix}, \quad (2.2)$$

with energies $E_{k,\pm} = \pm k$. Here, $k = |\mathbf{k}| = \sqrt{k_x^2 + k_y^2}$ and $\phi_{\mathbf{k}}$ is the polar angle characterizing \mathbf{k} . Since the $\hat{\mathcal{H}}$ exhibits translational symmetry along the y direction, the y momentum, k_y , remains a good quantum number. Considering only the subspace labeled by k_y , the Hamiltonian becomes:

$$\hat{h}(k_y) = \hat{h}_0(k_y) + \hat{V} \quad \text{with} \quad \hat{h}_0(k_y) = \sigma_x \hat{p}_x + \sigma_y k_y. \quad (2.3)$$

The energy eigenstates of $\hat{h}_0(k_y)$ can be rewritten as:

$$\psi_{\mathbf{k},\pm}(\mathbf{r}) = \frac{1}{\sqrt{L_y}} e^{ik_y y} \phi_{k_x}(x), \quad (2.4)$$

where $\phi_{k_x}(x)$ can be obtained by comparing with Equation (2.2) and satisfies the Schrödinger equation,

$$\hat{h}_0(k_y) \phi_{k_x}(x) = E_k \phi_{k_x}(x). \quad (2.5)$$

The energy spectrum of full Hamiltonian, $\hat{h}(k_y)$, can be found using the T-matrix approach. First, the Green's functions corresponding to the unperturbed and full Hamiltonians, \hat{h}_0 and \hat{h} , are respectively:

$$\hat{G}_0(\omega) = \frac{1}{\omega - \hat{h}_0} \text{ and } \hat{G}(\omega) = \frac{1}{\omega - \hat{h}}, \quad (2.6)$$

where ω is a complex frequency variable. \hat{G} is related to \hat{G}_0 through the T matrix:

$$\hat{G} = \hat{G}_0 + \hat{G}_0 \hat{T} \hat{G}_0, \text{ where } \hat{T} = \hat{V} + \hat{V} \hat{G}_0 \hat{T}. \quad (2.7)$$

All quantities are assumed to be functions of ω . The energy eigenvalues of the full Hamiltonian can be found from poles of operator $\hat{G}(\omega)$. These poles can correspond to poles coming from \hat{G}_0 (continuous spectrum) or from \hat{T} (isolated bound states). The energy of the one-dimensional bound state can thus be deduced from the poles of $\hat{T}(\omega)$.

Since the added defect corresponds to a delta function, one can show that $\langle x|\hat{T}|y\rangle$, expressed in the coordinate basis, must be of the form $t\delta(x)\delta(y)$. Using this representation in the defining Equation (2.7), one obtains:

$$\langle x|\hat{T}|y\rangle = \langle x|\hat{V}|y\rangle + \int dw dz \langle x|\hat{V}|w\rangle \langle w|\hat{G}_0|z\rangle \langle z|\hat{T}|y\rangle, \quad (2.8)$$

which simplifies to a simple relation between t and perturbation strength U :

$$t = \frac{U}{\mathbb{I} - U\langle 0|\hat{G}_0|0\rangle}. \quad (2.9)$$

Here \mathbb{I} is the identity matrix; $\langle 0|\hat{G}_0|0\rangle$ is the on-site Green's function:

$$\langle 0|\hat{G}_0|0\rangle = \sum_{k_x} \frac{\phi_{k_x}(0)\phi_{k_x}^\dagger(0)}{\omega - E_k} = \frac{1}{2\sqrt{k_y^2 - \omega^2}} \begin{pmatrix} -\omega & ik_y \\ -ik_y & -\omega \end{pmatrix}. \quad (2.10)$$

From Equation (2.9) one can see the poles of the T matrix must be zeroes of the denominator $\mathbb{I} - U\langle 0|\hat{G}_0|0\rangle$. Thus, the one-dimensional bound state energy ε_b is found by solving the determinant equation,

$$\det [\mathbb{I} - U\langle 0|\hat{G}_0(\varepsilon_b)|0\rangle] = 0, \quad (2.11)$$

which yields

$$\varepsilon_b = \frac{U^2 - 4}{U^2 + 4} \text{sgn}(U)|k_y|. \quad (2.12)$$

This is the promised linear dispersion relation converging to the Dirac point of surface band. For any strength U , the group velocity $d\varepsilon_b/dk_y$ has a magnitude smaller than 1 so the bound state is always in the energy gap at momentum k_y .

The dispersion is perfectly linear because Dirac cone of surface band is assumed to extend to infinite momentum. The bound state dispersion on the surfaces of realistic topological materials require the imposition of a finite energy band cutoff, usually provided by the bulk band gap. This corresponds to a high energy momentum cutoff, k_0 , in Equation (2.10). In that case one can find,

$$\langle 0|\hat{G}_0|0\rangle = \sum_{|k_x| < k_0} \frac{\phi_{k_x}(0)\phi_{k_x}^\dagger(0)}{\omega - E_k} = \frac{\arctan(k_0/\sqrt{k_y^2 - \omega^2})}{\pi\sqrt{k_y^2 - \omega^2}} \begin{pmatrix} -\omega & ik_y \\ -ik_y & -\omega \end{pmatrix}. \quad (2.13)$$

The bound state energy now has a correction term which is proportional to k_y^2 and inversely proportional to cutoff momentum k_0 :

$$\varepsilon_b = \frac{U^2 - 4}{U^2 + 4} \text{sgn}(U)|k_y| - \frac{128U^3k_y^2}{\pi(U^2 + 4)^3} \frac{1}{k_0} + o(1/k_0^2). \quad (2.14)$$

The quadratic correction to bound state energy makes the dispersion curve back down, which captures results obtained from simulations [41]. One can also even take the rotational symmetry of Dirac cone into account, so the cutoff can be made k_y -dependent: replacing $k_0 \rightarrow \sqrt{k_0^2 - k_y^2}$ in the result. Figure 2.2 shows the dispersion of scaled bound state energy ε_b/k_0 with respect to the scaled momentum, k_y/k_0 , in presence of cutoff $\sqrt{k_0^2 - k_y^2}$, for different values of the defect strength U .

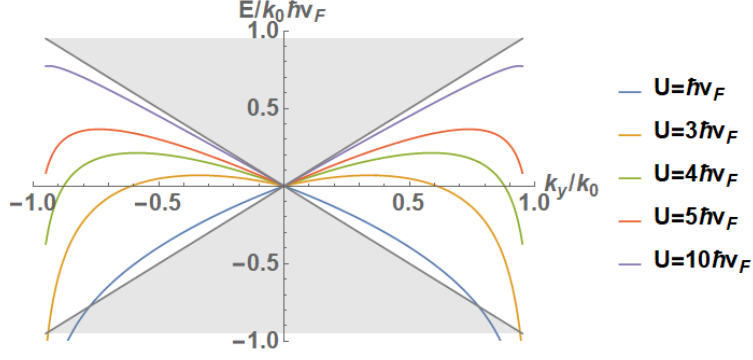


Figure 2.1. Bound state dispersion at line defect on surface of 3D TI without magnetic field, at different defect strength U . The band of bound states connects to the Dirac point of 2D surface states, with linear dispersion near the Dirac point, forming the connection topology. Finite cutoff momentum k_0 makes the dispersion curves back to surface band at large momentum. Shaded region is occupied by 2D surface states.

2.3 In Presence of Perpendicular Magnetic Field

I now proceed to break time reversal symmetry by turning on a magnetic field perpendicular to the 3D topological insulator surface. Time-reversal symmetry is broken, so the protected Kramers degeneracy at the surface Dirac point is also lifted. This phenomenon is captured by introducing a mass term in the low-energy Hamiltonian in Equation (2.1), with the mass being proportional to the magnetic field:

$$\hat{\mathcal{H}}_0 = \sigma_x \hat{p}_x + \sigma_y \hat{p}_y + m \sigma_z. \quad (2.15)$$

Eigenstates of the unperturbed Hamiltonian are

$$\psi_{\mathbf{k},\pm}(\mathbf{r}) = \frac{1}{\sqrt{2L_x L_y}} \frac{1}{\sqrt{m^2 + k^2 \mp m \sqrt{m^2 + k^2}}} e^{i\mathbf{k} \cdot \mathbf{r}} \begin{pmatrix} k e^{-i\phi_{\mathbf{k}}} \\ -m \pm \sqrt{m^2 + k^2} \end{pmatrix}, \quad (2.16)$$

with corresponding energies $E_k = \pm\sqrt{m^2 + k^2}$. Using the T-matrix method, subject to the condition $\omega^2 < m^2 + k_y^2$, $\langle 0|\hat{G}_0|0\rangle$ can be calculated analytically:

$$\langle 0|\hat{G}_0|0\rangle = \frac{\arctan(k_0/\sqrt{m^2 + k_y^2 - \omega^2})}{\pi\sqrt{m^2 + k_y^2 - \omega^2}} \begin{pmatrix} -\omega - m & ik_y \\ -ik_y & -\omega + m \end{pmatrix}. \quad (2.17)$$

k_0 is the cutoff momentum. The dispersion relation of 1D bound states is now found to be

$$\varepsilon_b = \frac{U^2 - 4}{U^2 + 4} \text{sgn}(U) \sqrt{m^2 + k_y^2} - \frac{128U^3(m^2 + k_y^2)}{\pi(U^2 + 4)^3} \frac{1}{k_0} + o(1/k_0^2). \quad (2.18)$$

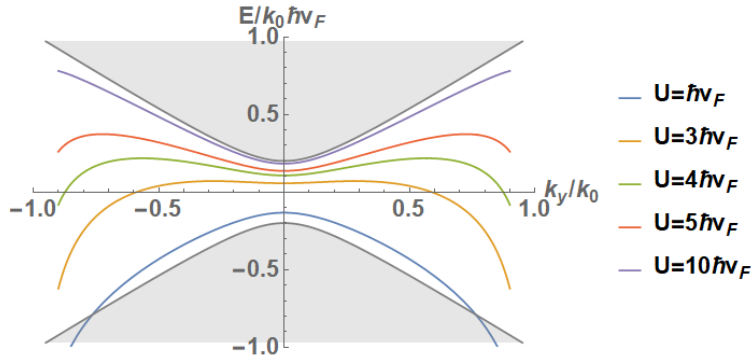


Figure 2.2. Bound state dispersion at line defect on surface of 3D TI in the presence of magnetic field, at different defect strength U . To model magnetic field, mass m is set to be $0.2k_0\hbar v_F$. Shaded region is occupied by 2D surface states.

Figure 2.2 shows the energy-momentum dispersions of the scaled bound state energy ε_b/k_0 , in presence of a k_y -dependent cutoff $\sqrt{k_0^2 - k_y^2}$, with different values of the defect strength U . Clearly, once the topological protection for the gaplessness of topological insulator surface states is removed by adding a magnetic field, the dispersion of the one dimensional defect bound mode is no longer tied to the Dirac point.

2.4 Summary

In this work the (2+1)-d Dirac fermion perturbed by a local one-dimensional potential was used to model the low-energy surface bands of a 3D topological insulator in presence

of step-edge-like surface line defect. I found the bound state dispersion and by finding the poles of the T matrix, the energy dispersion of 1D bound states localized at the defect was obtained. The dispersion was found to linearly converge to the Dirac point, featuring a connection topology as observed from recent studies [37], [38]. When the finiteness of band gap was taken into account, a momentum cutoff was included and it produced a quadratic correction in the energy dispersion. This analytical result agrees well with the simulation result [41]. I also explored how the connection between the Dirac point and the bound mode dispersion is broken when time reversal symmetry is violated by adding a magnetic field.

2.5 Chapter Acknowledgements

The content of this chapter has been published and appears in: “Connection topology of step edge state bands at the surface of a three dimensional topological insulator”, New J. Phys. **20**, 073014 (2018) [41].

3. 3D TOPOLOGICAL INSULATOR THIN FILMS WITH PARALLEL MAGNETIC FIELD

3.1 Introduction

3D topological insulators (TIs) have helical gapless surface states, whose gapless nature is protected by time reversal symmetry [25], [43]. Thus, ideal topological insulators are semimetals, not insulators, since each Dirac mode on the surface has been found to contribute a conductance of about $2e^2/h$. Breaking the gapless nature of these states in a controllable fashion will allow controlled transition between conducting and insulating states [24], [44], [45]. Such setups can underlie future switching technologies replacing conventional transistors. The process also allows one to investigate the nature of topological protection in topological insulators.

As discussed in the last chapter, turning on a magnetic field will gap the surface states by breaking time reversal symmetry. There is another route to doing this – by considering a thin film of the topological insulator, whose thickness is comparable to the bulk decay length of the surface states. Since surface states on opposite surfaces have opposite helicities, they can scatter off each other and open an energy gap at the Dirac point [17], [46].

In the following theoretical accompaniment to experimental studies of TI thin films, I will study the interplay between both aforementioned gap-opening processes in 3D TI thin films [47]. Surface energy gap opening and closing processes have been experimentally detected using transport measurements. First, I will analyze the gap-opening caused by hybridization between surface Dirac modes in thin films using a continuum theory. Next, I will analytically explain how an insulator-semimetal transition occurs when the thin film band structure is subjected to a parallel magnetic field. When hybridization exists, an insulator-semimetal transition driven by tuning the parallel magnetic field is observed, which has been previously predicted by other theoretical workers [48].

3.2 Hybridization of Surfaces of TI Thin Films

In Chapter 1 the boundary states of topological materials were found to exponentially decay from the interface and also the decay length was calculated from the bulk Hamiltonian. In a 3D TI film whose thickness is much larger than the decay length of surface states, there is no overlap between the surface states and they remain gapless. However, when the thickness of the film is reduced, such that it is smaller than or of the order of decay length, the surface states hybridize and an energy gap appears in the spectrum. Around the Dirac point, this finite thickness hybridization effect can be modeled by adding a tunneling term coupling the massless Dirac fermions, with opposite helicities, on the two surfaces [48]:

$$\hat{\mathcal{H}} = v_F \tau^z (\hat{z} \times \boldsymbol{\sigma}) \cdot \hat{\mathbf{p}} + \Delta_0 \tau^x. \quad (3.1)$$

Here, I have set $\hbar = 1$; v_F is the Fermi velocity; σ and τ are Pauli matrices acting on spin and surface degrees of freedom respectively; $\tau^z (\hat{z} \times \boldsymbol{\sigma}) \cdot \mathbf{p}$ is the Hamiltonian for two independent gapless Dirac fermions with opposite helicities; and $\Delta_0 \tau^x$ is a spin-conserving tunneling term. The energy spectrum of Hamiltonian (3.1) is doubly degenerate, with an energy gap of magnitude $2\Delta_0$ (one can choose $\Delta_0 > 0$ by adjusting the definition of τ):

$$E_{k,\pm} = \pm \sqrt{v_F^2 (k_x^2 + k_y^2) + \Delta_0^2}. \quad (3.2)$$

When the TI film thickness decreases, Δ_0 will increase due to increasing hybridization of opposite surfaces. Δ_0 should also depend on the energy, as one can deduce below. The thickness-dependence of the tunneling amplitude, Δ_0 , can be computed from matrix elements $\langle \psi_t | \hat{\mathcal{H}}_{\text{TI}} | \psi_b \rangle$, where $\psi_{t,b}$ are the wavefunctions of the top/bottom surface modes and $\hat{\mathcal{H}}_{\text{TI}}$ is the full TI Hamiltonian. $\psi_{t,b}$ have the same form as the eigenstates of Hamiltonian (3.1), multiplied by a decaying factor of the form $e^{-\lambda z_{t,b}}$, $z_{t,b}$ being the coordinates pointing into the bulk for either surface. Δ_0 thus depends on the film thickness, t , with an asymptotic behavior $e^{-\lambda t}$ for large t . $1/\lambda$ is an energy-dependent decay length whose energy-dependence can be modeled using Equations (1.21), (1.26).

In the following, I will adopt such an exponential dependence of Δ_0 on thickness, however, ignore the energy-dependence of λ since I will exclusively consider the value of Δ_0 around the neutrality point, where its dependence on energy is minimum. When the film thickness is reduced below $t \sim 1/\lambda$, Δ_0 increases rapidly and so do the energy gap and the mixing of the Dirac modes. This gap opening can be experimentally detected by measuring the drop in longitudinal conductivity in thinner and thinner TI films.

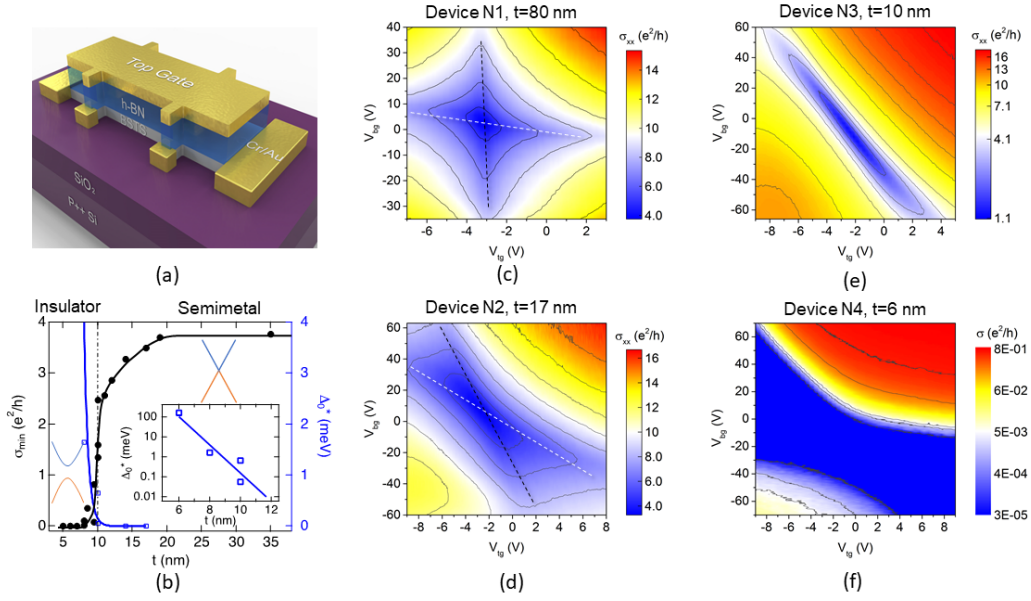


Figure 3.1. Conductivity measurement of BiSbTeSe₂ thin films. (a) Schematic of a dual-gated TI device. (b) σ_{\min} as function of thickness and the extracted Δ_0^* (to distinguish from theoretical Δ_0) from changing-temperature measurement. (c)-(f) Measured conductivity as function of gate voltages V_{tg}, V_{bg} . (c)-(e) at $T = 0.35K$ and (f) at $T = 1.6K$. (c) Semimetal phase. Black and white dashed lines show trace of Dirac points of top and bottom surfaces. They are parallel to y, x axes since the two surfaces are independent. (d) Crossover region. Slanted black and white traces of neutrality points indicate two surfaces start to hybridize. (e) Critical thickness. σ_{\min} drops below $4e^2/h$. (f) Insulating phase. Deep blue region shows nearly vanishing conductivity. This figure has been adapted from our publication [47].

In accompanying experiments [47], transport measurements were made on a sequence of BiSbTeSe₂ films with varying thickness, in the Hall-bar geometry. These devices had two gates, affecting the top and bottom surfaces of the film. Using such dual gating, the con-

ductivities of the top and bottom surfaces can be individually modulated through changing their carrier densities. The minimum conductivity, σ_{\min} , is achieved when two surfaces are gated simultaneously to charge neutrality point (see Figure 3.1). Thick samples ($t > 20\text{nm}$) yield σ_{\min} close to the value $4e^2/h$, corresponding to $2e^2/h$ per gapless Dirac modes. When the thickness is reduced to 17nm , hybridization becomes important as indicated by transport. When the thickness drops below 12nm , a proper energy gap opens in the surface bands which is indicated by nearly vanishing σ_{\min} region. Thus, we deduce that the critical thickness for the insulator-semimetal transition driven by surface hybridization is around 10nm in BiSbTeSe_2 . Independently, measuring σ_{\min} vs. temperature in the insulating state yields the energy gap, Δ_0 , also the thermal activation behavior, by fitting with the form $\sigma_{\min} \propto e^{-\Delta_0/2k_B T}$. The exponentially decaying relation $\Delta_0 \propto e^{-\lambda t}$ was verified in experiments.

3.3 Insulator-Semimetal Transition Driven By Parallel Magnetic Field

Applying a magnetic field parallel to an isolated TI surface does not change its physics much, since the vector potential introduced by magnetic field is equivalent to a gauge transformation on wavefunctions and results in a shift of the surface band in momentum space. In a thin film, such a magnetic field has a nonzero flux through the cross section of the film and so the vector potential fields at the top and bottom surfaces are not equal. Thus, the surface bands get shifted in opposite directions, creating a distance between their Dirac band structures in momentum space.

Assuming the parallel magnetic field is applied along x direction and choosing the Landau gauge $\mathbf{A} = -Bz\hat{y}$, the vector potentials at the two surfaces, whose locations are given by $z = \pm t/2$, are $\mp Bt\hat{y}/2$ respectively. Replacing $\mathbf{p} \rightarrow \mathbf{p} + e\mathbf{A}$ in Equation (3.1), the low energy effective Hamiltonian becomes [48]

$$\hat{\mathcal{H}} = v_F \tau^z (\hat{z} \times \boldsymbol{\sigma}) \cdot (\hat{\mathbf{p}} - \kappa_B \tau^z \hat{y}) + \Delta_0 \tau^x, \quad (3.3)$$

where $\kappa_B = t/2l_B^2$ is the ‘magnetic wave vector’, $l_B = \sqrt{c/eB}$ being the magnetic length.

One finds the energy eigenvalues to be $\pm\varepsilon_{\mathbf{k}\pm}$, where

$$\varepsilon_{\mathbf{k}\pm} = \sqrt{v_F^2(k_x^2 + k_y^2) + \varepsilon_B^2 + \Delta_0^2 \pm 2\varepsilon_B\sqrt{v_F^2k_y^2 + \Delta_0^2}}. \quad (3.4)$$

Here $\varepsilon_B = v_F\kappa_B$ is the ‘magnetic energy’. Since ε_+ and ε_- are interchanged if parallel magnetic field flips direction, one can assume $\varepsilon_B > 0$ in the following. When both Δ_0 and ε_B are nonzero, the spectrum is gapless at point(s) in momentum space satisfying the following conditions

$$k_x = 0, \quad \varepsilon_B = \sqrt{v_F^2k_y^2 + \Delta_0^2}. \quad (3.5)$$

Let’s consider the possibilities below.

The first case to consider is when the hybridization strength is stronger than the magnetic energy, $\Delta_0 > \varepsilon_B$. In this case conditions (3.5) cannot be satisfied, so the thin film remains insulating, similar to the extreme limit when there is no magnetic field. The valence and conduction bands are closest when $k_x = 0$ and $\sqrt{v_F^2k_y^2 + \Delta_0^2} - \varepsilon_B$ is minimized, i.e., at $\mathbf{k} = 0$.

Next, consider the critical case $\Delta_0 = \varepsilon_B$. This is a semimetal phase with single gapless point at the origin. Near $\mathbf{k} = 0$, $\varepsilon_- \sim v_F\sqrt{k_x^2 + (v_F^2/4\Delta^2)k_y^4}$, so the energy gap (between $\pm\varepsilon_-$) closes at $\mathbf{k} = 0$. Thus, at this value of the magnetic field, the energy gap initially opened by the hybridization process is closed again. Therefore by applying a parallel magnetic field one should expect an insulator-semimetal phase transition in 3D TI thin films.

Finally, when the magnetic field becomes larger, $\Delta_0 < \varepsilon_B$. One can find two Dirac points located at

$$k_y = \pm\sqrt{\kappa_B^2 - (\Delta_0/v_F)^2}. \quad (3.6)$$

In the strong field limit $\Delta_0 \ll \varepsilon_B$, these two Dirac points can be identified as the hybridization-free independent gapless Dirac fermions of opposite chiralities being shifted by $\pm\kappa_B\hat{y}$ in momentum space, as discussed previously. The hybridization, Δ_0 , considered as a perturbation which couples states at the same momentum value, is effective only at the intersection points between two un-hybridized surface bands. At these intersection points, new gaps of magnitude $2\Delta_0$ appear. As reasoned by [48], [49], the two Dirac points in strong field limit are also *topologically* protected and cannot be gapped by small surface hybridization. The two Dirac

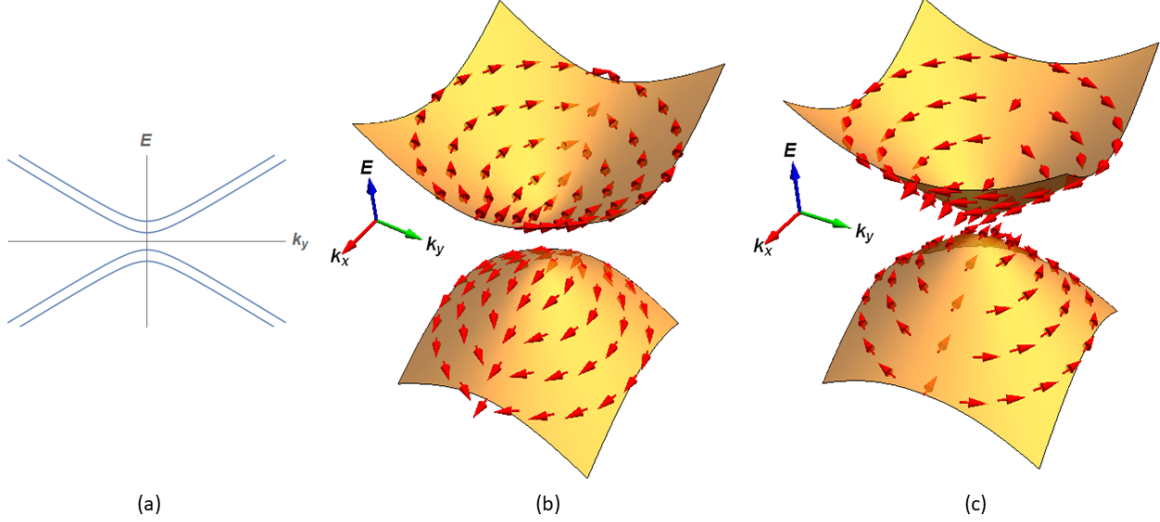


Figure 3.2. Insulating phase, $\Delta_0 > \varepsilon_B$. (a) Dispersion of bands along k_y direction. (b),(c) Band structure and spin texture of top, bottom bands and two middle bands. The spin texture arrows show averages of three spin components of a state, $\langle s_x \rangle$, $\langle s_y \rangle$, $\langle s_z \rangle$, where $\langle s_i \rangle$ ($i = 1, 2, 3$) of a state ϕ is defined as $\langle \phi | \tau_0 \otimes \sigma_i | \phi \rangle$ with τ_0 the identity matrix acting on surface degree of freedom. From spin texture plot one can see the four insulating bands have zero helicity.

cones, separated in momentum space, both have definite helicities. Hybridization processes with zero momentum transfer, which fail to couple states with opposite helicities, cannot destroy the gapless points because helicity, a discrete quantity, cannot be continuously destroyed, which it needs to be in order to produce an insulating band which must have zero helicity due to continuity of spin texture in momentum space.

When the Dirac points coincide at the critical parameter values $\Delta_0 = \varepsilon_B$, this protection can no longer operate due to the hybridization of the two opposite helicities. Thus, a gap can begin to open near this point in parameter space. If Δ_0 keeps increasing beyond this value, the hybridization gap opens and has a ‘compensated’ form $2(\Delta_0 - \varepsilon_B)$. Figures 3.2, 3.3, 3.4 show plots of the band structure and spin texture of the four bands in the three cases discussed above.

Our theoretical analysis qualitatively agrees with the corresponding experimental results [47]. The energy band gap of 3D TI thin films, in the presence of a parallel magnetic field, was detected through magnetoresistance (MR) measurements (Figure 3.5). For thin films of

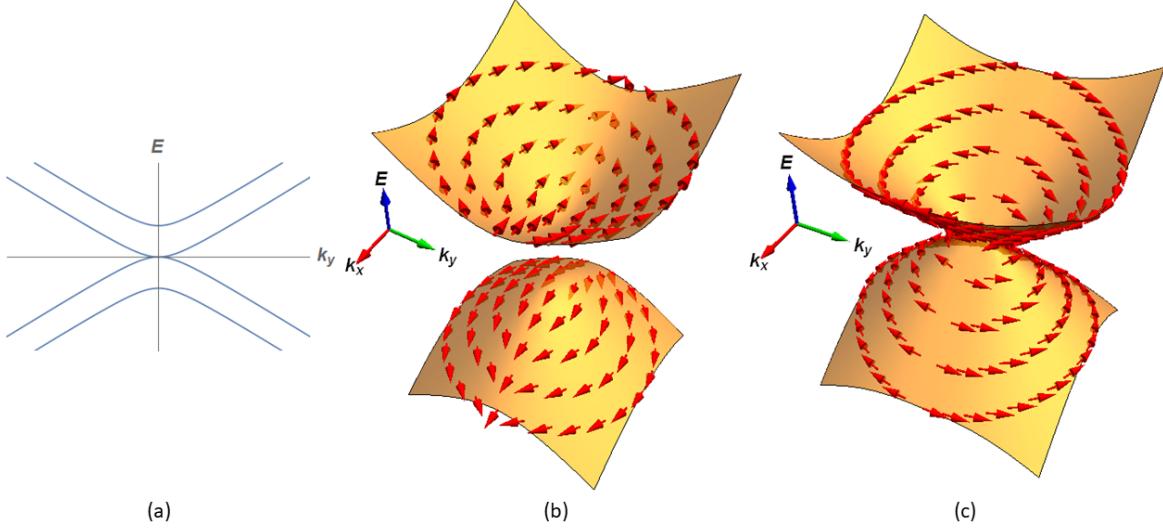


Figure 3.3. Critical semimetal phase, $\Delta_0 = \varepsilon_B$. (a) Dispersion of bands along k_y direction. (b) Top and bottom insulating band. (c) Two middle bands touch at a gapless point. k_x axis is a nodal line for the spin texture, and on its two sides the pattern of two Dirac cones are preserved (see Fig). Spin vector vanishes along the nodal line, since the spin here is defined as overall spin of both surfaces. Vanishing spin vector means these on two surfaces exactly cancel each other.

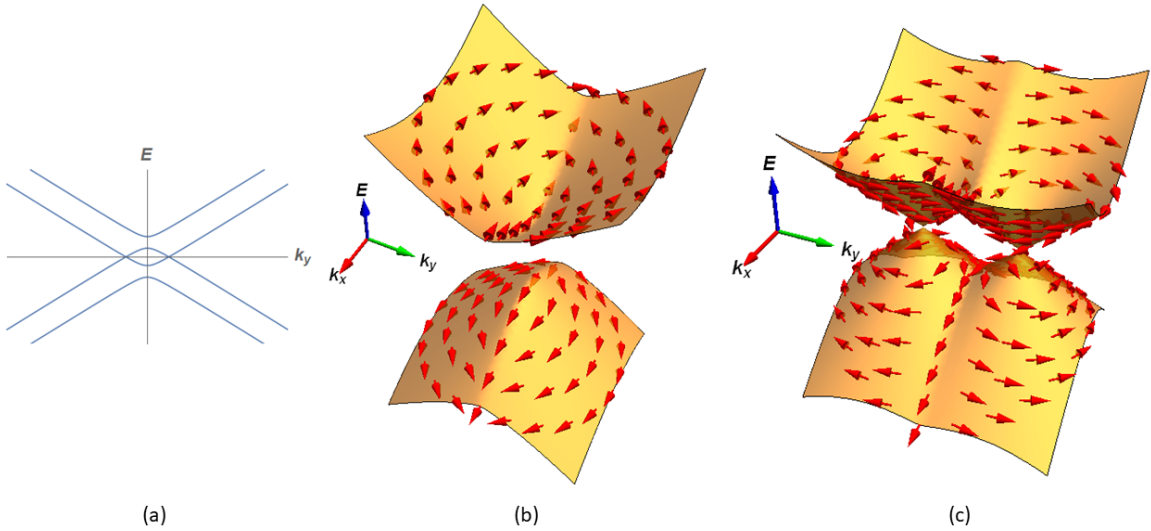


Figure 3.4. Dirac-Weyl semimetal phase, $\Delta_0 < \varepsilon_B$. (a) Dispersion of bands along k_y direction. (b) Top and bottom insulating bands. (c) Two middle bands touch at two Dirac points with helicity ± 1 .

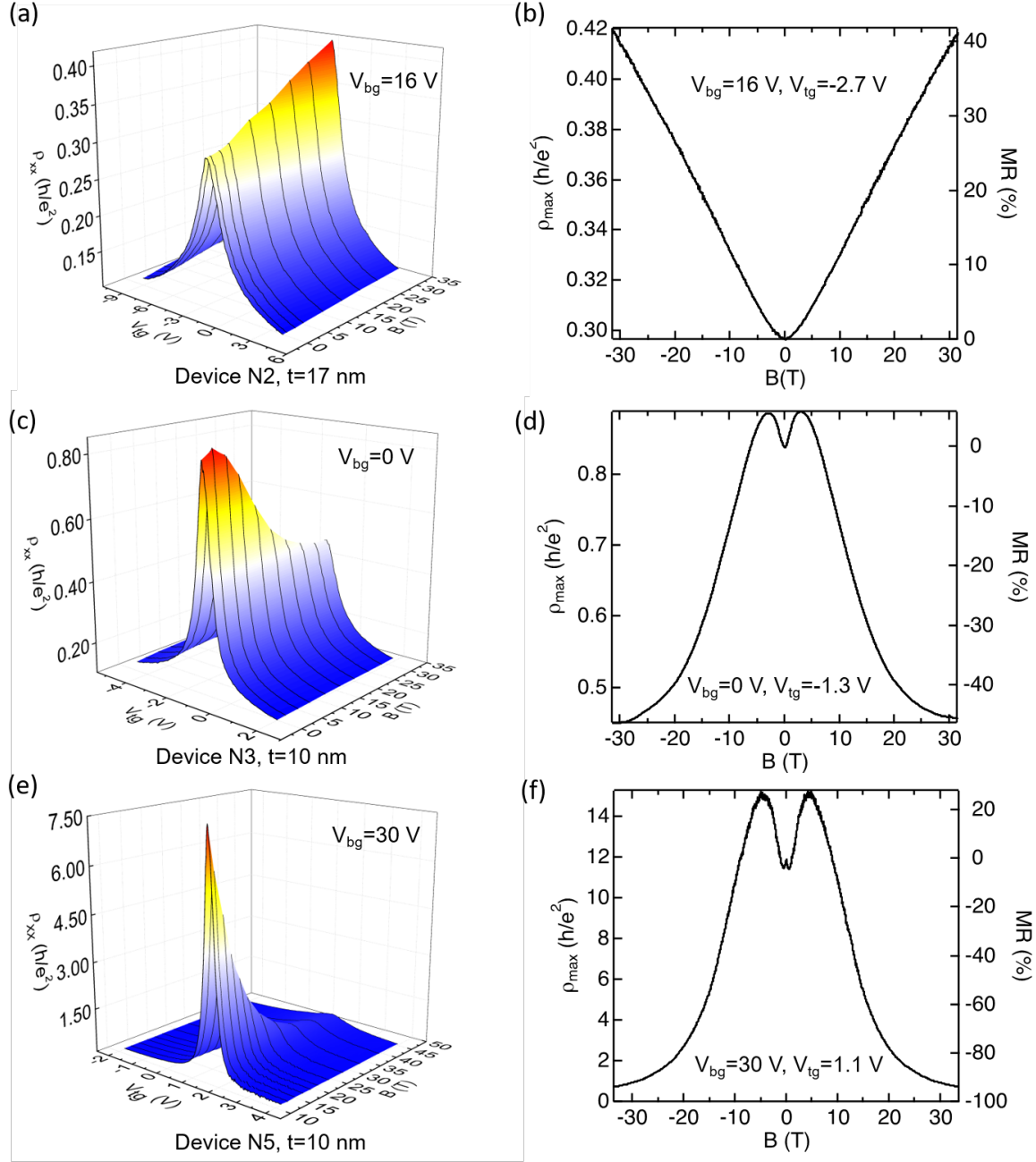


Figure 3.5. Magnetoresistance measurement of 3D TI thin films. (a),(c),(e) Resistivity measurement of three devices as a function of V_{tg} and parallel B field. V_{bg} is fixed at chosen values such that sweeping V_{tg} will pass through $\rho_{max} = 1/\sigma_{min}$. (b),(d),(f) ρ_{max} and MR as functions of parallel B field, at fixed V_{tg} and V_{bg} . This figure has been adapted from our publication [47].

relatively large thickness ($t = 17\text{nm}$) where Dirac nodes have not been destroyed by surface hybridization, small resistivity and small positive MR values were observed, indicating the stability of gapless surface Dirac nodes against the parallel magnetic field. For thinner films with substantial surface hybridization and energy gaps, increasing parallel magnetic field closes the energy gap, causing an insulator-semimetal phase transition and resulting in negative MR values. In some cases, some positive MR values near the low field region were also observed. These disappear when increasing temperature and we believe that they are attributed to phase coherent transport [50], [51].

3.4 Summary

As discussed in the last chapter, turning on a magnetic field allows us to gap the surface states by breaking time reversal symmetry. There is another route to doing this – by considering a thin film of the topological insulator, whose thickness is comparable to the bulk decay length of the surface states. Since surface states on opposite surfaces have opposite helicities, they can scatter off each other and open an energy gap at the Dirac point [17], [46].

We presented a theoretical explanation of experimental studies of TI thin films studying the interplay between two kinds of gap-opening processes in 3D TI thin films [47] – surface state hybridization and parallel magnetic fields. We analyzed, using both continuum theory and topological arguments, the gap-opening and closing processes caused by a competition between (a) the hybridization of surface Dirac modes in thin films and (b) the momentum space separation of the two Dirac nodes by a parallel magnetic field, which prevents hybridization from affecting them. These conclusions have been validated in temperature and dual gate-tuned transport measurements in 3D topological insulator (BiSbTeSe_2) films with varying thicknesses [47].

3.5 Chapter Acknowledgements

The content of this chapter has been published and appears in: “Tuning insulator-semimetal transitions in 3D topological insulator thin films by intersurface hybridization and in-plane magnetic fields”, Phys. Rev. Lett. **123**, 207701 (2019) [[47](#)].

4. TOPOLOGICAL GRAVITATIONAL RESPONSE IN TWO-DIMENSIONAL TOPOLOGICAL MATERIALS

4.1 Introduction

Since the discovery of quantum Hall effect it has been known there exists a class of material properties which can only assume discrete values and are thus precisely fixed over finite range of material parameters. The physics of these quantized properties are explained using topological arguments, such as the Chern number formulation for Hall conductance relates the quantization of the Hall conductance to the discreteness of electron charge and the principle of gauge invariance [2], [8], [52].

The Hall conductance is a well-known but rare example of measurable material property that is topologically quantized (can be zero!) in a wide class of materials, viz., in all two-dimensional insulating states of matter. Herein I consider another apparently quantized property of quantum Hall states, the gravitational coupling constant (GCC). The GCC characterizes linear charge response to spatial curvature, as theoretically predicted by Wen and Zee when studying the effects of space-time deformations, i.e., gravity, to the Chern-Simons field theories describing quantum Hall states [53]. This is the reason why the phrase ‘gravitational response’ is used.

In this work I establish that quantized gravitational response occurs in a wide class of two dimensional topological quantum states on the lattice – I call this ‘topological gravitational response’, or TGR for short. Unlike in continuous space, only discrete singular values of Gaussian curvature can be realized on the lattice [54]. Specifically, lattice disclinations carry Gaussian curvature (equal to the Frank angle of the disclination) and our TGR formulation describes how fractional charges accumulate at such disclinations in a universal fashion that only depends on the disclination curvature and the topological properties of the topological phase being studied. Extending calculations involving quantum Hall states on a lattice reported before [54], I will describe how to adapt any flat-lattice tight binding model to a lattice with a disclination and implement well-known models Chern insulators and topological insulators on these lattice disclinations to study and demonstrate TGR.

I will first describe the construction of some paradigmatic Chern insulator models around disclinations, calculate their spectra and report observations of quantized fractional charges at these disclinations. I will finally close with analysis that extracts the universal part of this response, establishing TGR in these models.

4.2 Tight-binding Calculation of Disclination Charge

I will use the tight-binding method to calculate the energy spectrum and charge density in topological systems [55]. The general tight-binding Hamiltonian for a lattice system has the form

$$\hat{\mathcal{H}} = \sum_{\mathbf{R}, \boldsymbol{\delta}} \hat{\Psi}^\dagger(\mathbf{R} + \boldsymbol{\delta}) t(\boldsymbol{\delta}) \hat{\Psi}(\mathbf{R}). \quad (4.1)$$

Here, \mathbf{R} is a vector labeling positions of unit cells. $\hat{\Psi}^\dagger(\mathbf{R})$ and $\hat{\Psi}(\mathbf{R})$ are d -dimensional vectors whose components are creation and annihilation operators of internal degrees of freedom, e.g. sublattices and spins, inside the Bravais unit cell at location \mathbf{R} . $t(\boldsymbol{\delta})$ are d -dimensional hopping matrices prescribing hopping amplitudes between cells connected by the hopping vectors $\boldsymbol{\delta}$. Of course, the model is explicitly translation invariant and so is defined on a lattice, i.e., on flat space. Diagonalizing the tight-binding Hamiltonian yields energy the spectrum and wavefunctions of single-electron eigenstates. When these single-electron states are filled up to some Fermi level E_F not coinciding with the energy of any state, the local charge density within a unit cell is given by formula

$$\rho(\mathbf{R}) = \sum_{E < E_F} \sum_{\alpha=1}^d |\psi^{(E)}(\mathbf{R}, \alpha)|^2. \quad (4.2)$$

$\psi^{(E)}$ denote energy eigenstate(s) with energy E and the internal degree of freedom is labeled by α . For clean topological band insulators on an infinite lattice, there is a clear bulk band gap and when the Fermi level is placed in the gap, $\rho(\mathbf{R})$ should be everywhere equal, yielding the ‘filling factor’ ν . A band insulator with the Fermi level inside the gap separating k valence bands from the conduction bands, the number of electrons is $\nu = k$ per Bravais unit cell. If the unit cell has multiple lattice points (hence equivalent), this charge is evenly distributed among them. If the lattice has a finite boundary or point defect, the tails of in-gap edge

states or impurity bound states can shift the local density from the above-mentioned value of ν . However, sum of the discrepancies along an edge or around a point defect should give an *integer* excess charge, which is equal to the number of filled edge states or impurity bound states. The excess charge is defined as [56]

$$\delta Q = \sum_{\tilde{\mathbf{R}}} [\rho(\tilde{\mathbf{R}}) - \nu] \quad (4.3)$$

where $\tilde{\mathbf{R}}$ goes over all sites near the edge or point defect. Around usual (non-topological) defects on flat lattices, this quantity is an *integer*.

For topological materials on curved lattices, i.e., in the presence of disclinations, δQ need not be an integer. Indeed, discarding the effects of non-universal aspects arising from disorder and vacancies, one can see that only the fractional part of δQ can be universal. Firstly, one notices that translation symmetry is broken and Hamiltonian (4.1) needs to be redefined. For elementary models with simple hopping amplitudes this redefinition can be straightforward, however for others it needs to be consistent with all symmetries of the flat space Hamiltonian. I have developed a systematic method for constructing tight-binding Hamiltonians around disclinations on a lattice with n -fold rotation symmetry (Appendix), utilizing the n -fold rotation symmetry obeyed by the flat space Hamiltonian.

I will now provide examples of three prototype tight-binding models around disclinations: the Haldane model Chern insulator on the honeycomb lattice, the QWZ Chern insulator on the square lattice and the Kane-Mele time reversal invariant topological insulator on the honeycomb lattice.

4.2.1 The Haldane Model

The Haldane model was the first Chern insulator model proposed [9] – it exhibits the quantized Hall effect in the absence of a net external magnetic field, the so-called quantum anomalous Hall effect (QAHE). The Hamiltonian is

$$\hat{\mathcal{H}} = \sum_{\mathbf{i}} M_{\mathbf{i}} \hat{c}_{\mathbf{i}}^{\dagger} \hat{c}_{\mathbf{i}} + t_1 \sum_{\langle \mathbf{ij} \rangle} \hat{c}_{\mathbf{i}}^{\dagger} \hat{c}_{\mathbf{j}} + t_2 (e^{i\phi} \sum_{r.t. \langle \langle \mathbf{ij} \rangle \rangle} \hat{c}_{\mathbf{i}}^{\dagger} \hat{c}_{\mathbf{j}} + h.c.), \quad (4.4)$$

where $M_i = \pm M$ are onsite masses for A/B sublattices; $\hat{c}_i^\dagger, \hat{c}_i$ are creation and annihilation operators at site i ; t_1, t_2 denote nearest- and second-nearest-neighbor ($\langle \rangle$ and $\langle\langle \rangle\rangle$, respectively) hopping amplitudes; $r.t.$ indicates second nearest-neighbor hops realized with one right-turn; ϕ is a tunable phase capturing a time reversal breaking staggered internal magnetic flux which is crucial for achieving QAHE. The Haldane model has two topological phases with Chern numbers $C = \pm 1$ [9], which are determined by condition

$$|M| < 3\sqrt{3}|t_2| \sin \phi \quad (4.5)$$

and separated by two nodes at $\phi = 0$ and π . The phase diagram is shown in Figure 4.1.

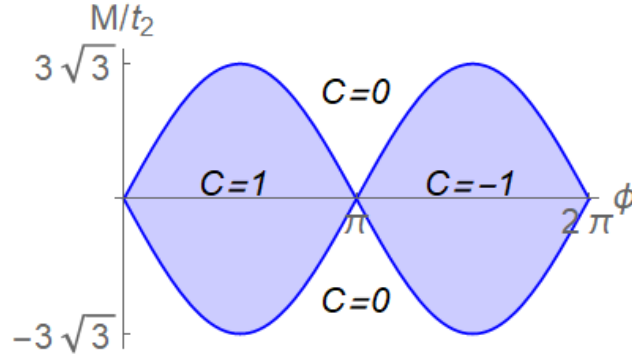


Figure 4.1. Phase diagram of Haldane model [9].

The behavior of the Haldane model at disclinations has been discussed by others [57]. On the hexagonal lattice one can choose various Wyckoff positions in hexagon as disclination center, so different types of disclinations can be created [58]. I will focus on the center-type and vertex-type disclinations of hexagonal lattice, which have 6-fold and 3-fold rotation symmetries respectively (Figure 4.2). Using the cut-and-glue process [59] (Figure 4.3), one breaks the flat hexagonal lattice into sectors, with each sector having an apical angle of $\pi/3$ or $2\pi/3$ depending on the disclination type. Removing or adding extra sectors lead to disclinations with positive or negative curvatures. Since the hopping amplitudes of the Haldane model are unchanged under rotations, two boundaries of the seam can be naturally joined without any further rotational gauge transformation. Using formula (4.3), excess charges of the two disclination types are calculated in Table 4.1 and 4.2.

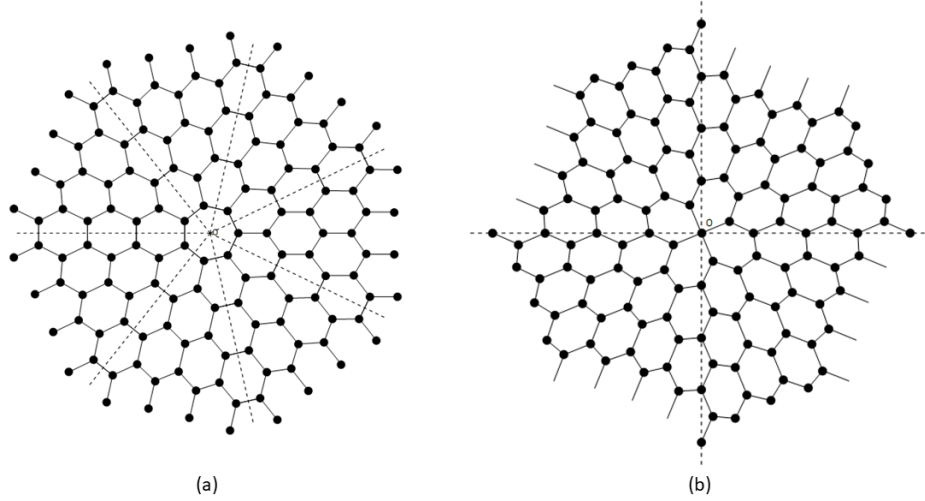


Figure 4.2. (a) Center-type and (b) vertex-type disclination of hexagonal lattice.

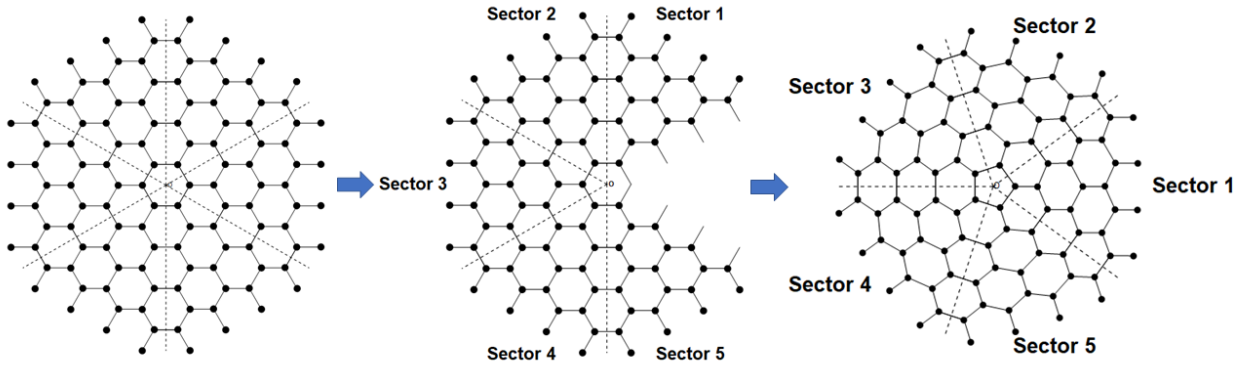


Figure 4.3. Cut-and-glue process to join a 5-sector center-type disclination of hexagonal lattice.

The calculation provides following important information for disclination charge of Haldane model. The excess charge is nonzero for both topological phases $C = \pm 1$ and zero for trivial phase $C = 0$. Within the same topological phase, e.g. $C = 1$, its fractional part is quantized and stable against tuning parameters within the phase. When phase ϕ changes sign, i.e., under time reversal, the disclination charge should remain the same because charge is even under time-reversal. Thus, phases $C = \pm 1$ have the same disclination charges. Lastly, the fractional part of the excess charges is proportional to the integrated curvature of the disclinations, which is an analogous result to the Hall fluid in continuous

space [53] and Hofstadter model on polyhedrons [54]. Finally, I find that the excess charges at site-centered disclinations depend on whether there is an atom at the center. Since at half-filling every atom contributes $1/2$ electron-charge, such vacancies can change all charges by integer multiples of $1/2$. However, the GCC, or the linear response coefficient, will be unaffected. This physics is incorporated in our universal formulation of TGR, presented in a later section.

Table 4.1. Excess charge of Haldane Model, center-type disclination, $C = \pm 1$ phase.

Number of sectors m	1	2	3	4	5	6	7	8	κ
Singular curvature/ 2π	5/6	2/3	1/2	1/3	1/6	0	-1/6	-1/3	
$[\delta Q_H^{\text{center}}]_{\text{frac}}$	3/4	0	1/4	1/2	3/4	0	1/4	1/2	-3/2

Table 4.2. Excess charge of Haldane Model, vertex-type disclination, $C = \pm 1$ phase.

Number of sectors m	1	2	3	4	5	κ
Singular curvature/ 2π	2/3	1/3	0	-1/3	-2/3	
$[\delta Q_H^{\text{vertex}}]_{\text{frac}}^\dagger$	0	0	0	0	0	0

4.2.2 The QWZ Model

The QWZ model is a prototype two-band Chern insulator model on the square lattice [12]. Its Hamiltonian is

$$\hat{\mathcal{H}} = \sum_{ij} \hat{\Psi}_{i,j}^\dagger m \sigma_3 \hat{\Psi}_{i,j} + \hat{\Psi}_{i+1,j}^\dagger \frac{\sigma_3 + i\sigma_1}{2} \hat{\Psi}_{ij} + \hat{\Psi}_{i,j+1}^\dagger \frac{\sigma_3 + i\sigma_2}{2} \hat{\Psi}_{ij} + h.c., \quad (4.6)$$

where i, j are the integer-valued x and y coordinates; $\hat{\Psi}_{ij}^\dagger, \hat{\Psi}_{ij}$ are 2-dimensional vectors whose components are the creation/annihilation operators corresponding to the two orbital states at site (i, j) ; m is the onsite mass gap and σ_i ($i = 1, 2, 3$) are Pauli matrices. This system can exist in two possible topological phases, with $C = \pm 1$ (corresponding to $-2 < m < 0$ and $0 < m < 2$, respectively), and the trivial phase with $C = 0$ (for $|m| > 2$).

The flat space QWZ Hamiltonian, unlike the Haldane model Hamiltonian, cannot be directly applied to lattices with disclinations since the hopping matrices are not equal in

different directions related by rotational symmetry. Choosing Bravais lattice vectors $\mathbf{a}_1 = (1, 0)$ and $\mathbf{a}_2 = (0, 1)$, the hopping vector $\boldsymbol{\delta}$ can take four different values $\pm\mathbf{a}_1, \pm\mathbf{a}_2$. The hopping matrices along these four directions are

$$t(\mathbf{a}_1) = t(-\mathbf{a}_1)^\dagger = \frac{\sigma_3 + i\sigma_1}{2}, \quad t(\mathbf{a}_2) = t(-\mathbf{a}_2)^\dagger = \frac{\sigma_3 + i\sigma_2}{2}. \quad (4.7)$$

It is found that they are related to each other by a rotation-dependent unitary operation:

$$t(R\boldsymbol{\delta}) = Ut(\boldsymbol{\delta})U^{-1}, \quad \text{with } U = e^{i\eta} \begin{pmatrix} 1 & 0 \\ 0 & i \end{pmatrix}, \quad (4.8)$$

where R is counterclockwise rotation of 90° and $\boldsymbol{\delta}$ is among the four values. η is an undetermined phase depending on the angular momentum of orbitals. For ‘Bosonic’ rotations, $U^4 = 1$ so η is an integer multiple of $\pi/2$. Fourier transforming the Hamiltonian to momentum space, $h(\mathbf{k})$, rotational invariance (4.8) can also be seen from relation

$$h(R\mathbf{k}) = Uh(\mathbf{k})U^{-1}. \quad (4.9)$$

The preceding analysis suggests that I can use the cut-and-glue process only after performing a unitary gauge transformation on one side of the seam. After the transformation, hopping matrices across the seam can be naturally defined. More details are provided in Appendix B. This way of defining the disclination Hamiltonian has the merit that away from the disclination core, it is everywhere equivalent to the flat space Hamiltonian. In other words, if one picks out a random patch away from the disclination core, including across the seam, Hamiltonian of the patch will be equivalent to the flat lattice Hamiltonian of QWZ model up to a unitary transformation. Another way of showing this is by observing that an additional gauge transformation can make the disclination Hamiltonian periodic, where the joined seam has no difference from any other nodal line between neighboring sectors. I have also provided a proof of this periodic property in Appendix C.

I calculated the excess charges on the center and vertex-type square lattice disclinations, they are sketched in Figure 4.4. Similar to the Haldane model, the disclination charge of

QWZ model is found to be nonzero only in the topological phases $C = \pm 1$. The excess charge also depends on the angular momentum of orbitals because the boundary conditions are η -dependent. For disclination Hamiltonians with different η values, an alternative way of thinking is to imagine the angular momentum of orbitals is unchanged but with a magnetic flux inserted through the disclination center, so the change of excess charges can be interpreted from Laughlin's argument [2]. This physics will be incorporated in our later section describing TGR.

Taking η as a control and comparing disclinations at different curvatures, the fractional excess charges are found to be proportional to the disclination curvature. The excess charges for $C = \pm 1$ phases with four different η values and two disclination types of square lattices are listed in Table 4.3, 4.4, 4.5 and 4.6.

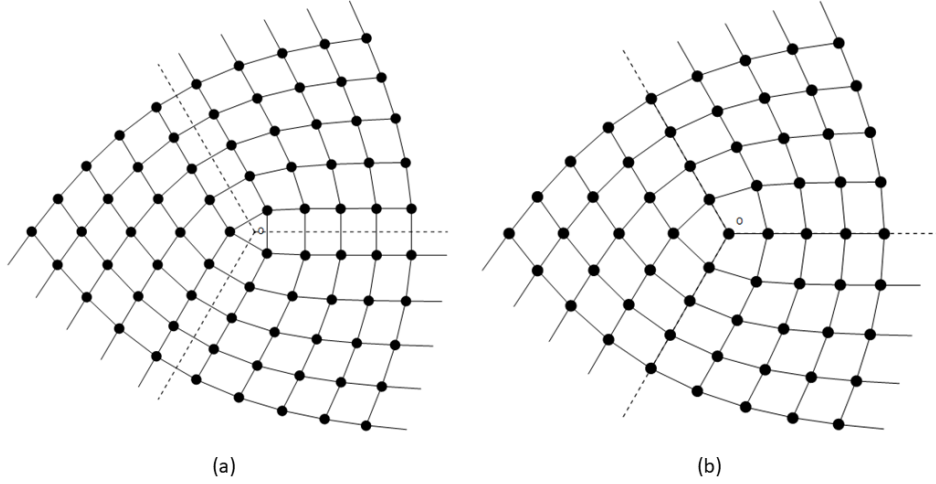


Figure 4.4. (a) Center-type and (b) vertex-type disclination of square lattice.

Table 4.3. Excess charge of QWZ model, center-type disclination, $C = 1$ phase.

Number of sectors m		1	2	3	4	5	6	7	κ
Singular curvature/ 2π		$3/4$	$1/2$	$1/4$	0	$-1/4$	$-1/2$	$-3/4$	
$[\delta Q_{QWZ}^{\text{center}}]_{\text{frac}}$	$\eta = 0$	$5/8$	$3/4$	$7/8$	0	$1/8$	$1/4$	$3/8$	$-1/2$
	$\eta = \pi/2$	$7/8$	$1/4$	$5/8$	0	$3/8$	$3/4$	$1/8$	$-3/2$
	$\eta = \pi$	$1/8$	$3/4$	$3/8$	0	$5/8$	$1/4$	$7/8$	$-5/2$
	$\eta = 3\pi/2$	$3/8$	$1/4$	$1/8$	0	$7/8$	$3/4$	$5/8$	$1/2$

Table 4.4. Excess charge of QWZ model, center-type disclination, $C = -1$ phase.

Number of sectors m		1	2	3	4	5	6	7	κ
Singular curvature/ 2π		3/4	1/2	1/4	0	-1/4	-1/2	-3/4	
$[\delta Q_{QWZ}^{\text{center}}]_{\text{frac}}$	$\eta = 0$	7/8	1/4	5/8	0	3/8	3/4	1/8	-3/2
	$\eta = \pi/2$	5/8	3/4	7/8	0	1/8	1/4	3/8	-1/2
	$\eta = \pi$	3/8	1/4	1/8	0	7/8	3/4	-3/8	1/2
	$\eta = 3\pi/2$	1/8	3/4	3/8	0	5/8	1/4	7/8	3/2

Table 4.5. Excess charge of QWZ model, vertex-type disclination, $C = 1$ phase.

Number of sectors m		1	2	3	4	5	6	7	κ
Singular curvature/ 2π		3/4	1/2	1/4	0	-1/4	-1/2	-3/4	
$[\delta Q_{QWZ}^{\text{vertex}}]_{\text{frac}}$	$\eta = 0$	5/8	3/4	7/8	0	1/8	1/4	3/8	-1/2
	$\eta = \pi/2$	7/8	1/4	5/8	0	3/8	3/4	1/8	-3/2
	$\eta = \pi$	1/8	3/4	3/8	0	5/8	1/4	7/8	-5/2
	$\eta = 3\pi/2$	3/8	1/4	1/8	0	7/8	3/4	5/8	1/2

Table 4.6. Excess charge of QWZ model, vertex-type disclination, $C = -1$ phase.

Number of sectors m		1	2	3	4	5	6	7	κ
Singular curvature/ 2π		3/4	1/2	1/4	0	-1/4	-1/2	-3/4	
$[\delta Q_{QWZ}^{\text{vertex}}]_{\text{frac}}$	$\eta = 0$	3/8	1/4	1/8	0	7/8	3/4	-3/8	1/2
	$\eta = \pi/2$	1/8	3/4	3/8	0	5/8	1/4	7/8	3/2
	$\eta = \pi$	7/8	1/4	5/8	0	3/8	3/4	1/8	-3/2
	$\eta = 3\pi/2$	5/8	3/4	7/8	0	1/8	1/4	3/8	-1/2

For square lattice both the center and vertex of square have four-fold rotation symmetry, but comparing Table 4.3 and 4.5, 4.4 and 4.6, one notices the GCC κ of different η values are shifted. This is resolved by noting that they correspond to different values of η , which non-topological dependence needs to be removed from the definition of TGR. I address this in a later section.

4.2.3 The Kane-Mele Model

In 2005 Kane and Mele proposed the first 2D topological insulator model on the honeycomb lattice [10], [11]. This model stacks two Haldane models with opposite Chern numbers,

$C = \pm 1$, and couples them with a Rashba term. This construction is constrained by imposing time reversal symmetry. The Hamiltonian is:

$$\hat{\mathcal{H}} = t_1 \sum_{\langle ij \rangle} \hat{\Psi}_i^\dagger \hat{\Psi}_j + t_2 (e^{is_z \phi} \sum_{r.t. \langle ij \rangle} \hat{\Psi}_i^\dagger \hat{\Psi}_j + h.c.) + i\lambda_R \sum_{\langle ij \rangle} \hat{\Psi}_i^\dagger (\mathbf{s} \times \hat{\mathbf{d}}_{ij})_z \hat{\Psi}_j. \quad (4.10)$$

Here I use a slightly different Hamiltonian from the original Kane-Mele model, explicitly retaining the phase ϕ of the Haldane model and eliminating the mass term, which breaks the sixfold rotation symmetry. Apart from the last Rashba term which couples the two spin layers, the Hamiltonian looks similar to Haldane model except $\hat{c}_i^\dagger, \hat{c}_i$ are replaced with 2-dimensional vectors $\hat{\Psi}_i^\dagger, \hat{\Psi}_i$ which have taken into account the two spin species. $\mathbf{s} = (s_x, s_y, s_z)$ are Pauli matrices acting on spin space, and $\hat{\mathbf{d}}_{ij}$ is the unit vector along a nearest-neighbor-hopping bond.

Due to the presence of time-reversal symmetry, pairs of gapless counter-propagating modes of opposite spins always exist along the edge and connect the valence and conduction bands [10], [11]. Therefore when voltage is applied, there is no net charge current but only spin current at the edge, yielding the so-called quantum spin Hall effect (QSHE). The topological trivial or nontrivial phases are characterized by even or odd number of pairs of counter-propagating edge modes, so fit into the \mathbb{Z}_2 classification of topological materials [60][61].

The Kane-Mele model cannot be implemented on disclinations directly due to the presence of non-identical Rashba couplings in different directions. To apply the cut-and-glue technique, a unitary transformation acting in spin space is needed to join the seam.

To do this, let us express $\hat{\mathbf{d}}_{ij}$ in the Rashba term as $(\cos \alpha, \sin \alpha)$, where α is the polar angle of bond \mathbf{d}_{ij} . Then, the Rashba hopping matrix is

$$t(\alpha) = (\mathbf{s} \times \hat{\mathbf{d}}_{ij})_z = s_x \sin \alpha - s_y \cos \alpha. \quad (4.11)$$

It is clear that under 60° rotation the matrices are related by following transformation:

$$t(\alpha + \frac{\pi}{3}) = Ut(\alpha)U^{-1}, \text{ with } U = e^{i\eta}e^{-is_z\frac{\pi}{3}} = e^{i\eta} \begin{pmatrix} e^{-i\pi/6} & 0 \\ 0 & e^{i\pi/6} \end{pmatrix}, \quad (4.12)$$

where η is a phase depending on the spin of two layers. Traditionally, the Kane-Mele model is thought of as composed of spin-up and -down of spin-1/2 fermions and so η can be an integer multiple of $\pi/3$. I use the same approach as for QWZ model to join the boundaries of seam, with the only difference being that now the gauge transformation takes place on two spin layers instead of two orbitals.

With the disclination Hamiltonian of Kane-Mele model defined, the excess charge can be computed. They are found to be proportional the disclination curvature, but independent of η . This can be understood from Laughlin's argument, since change of η is equivalent to flux insertion at disclination center, which induces zero net charge because the Kane-Mele model has the net Chern number value $C = 0$. Excess charges at center-type disclinations with different curvatures are given in Table 4.7: Only charges for QSH phase $0 < \phi < \pi$

Table 4.7. Excess Charge of Kane-Mele Model, center-type disclination, QSH phase $0 < \phi < \pi$.

Number of sectors m	1	2	3	4	5	6	7	8	κ
Total Curvature/ 2π	5/6	2/3	1/2	1/3	1/6	0	-1/6	-1/3	
$[\delta Q_{KM}^{\text{center}}]_{\text{frac}}$	1/3	2/3	0	1/3	2/3	0	1/3	2/3	-2

are listed. For the other phase $-\pi < \phi < 0$, the two layers are switched but the fictitious magnetic flux inserted by U matrix is the same, so disclination charges will change sign.

To understand the charge Table 4.7 from a microscopic point of view, I first consider the Kane-Mele model without Rashba coupling, which becomes just two independent Haldane models with $C = \pm 1$. Such a system preserving time-reversal symmetry is not unique, since one can insert fictitious magnetic flux Φ_0 through layer $C = 1$ and $-\Phi_0$ through layer $C = -1$. Applying Laughlin's argument to the two layers separately, one would find they give equal contributions to the disclination charge, so the charge would depend on Φ_0 . However, when Rashba term is turned on, it implies additional constraints on rotational invariance

(4.12) which requires that the fluxes through two layers must differ by $\pi/3$, plus some other external flux η which has no effect on total charge. Therefore, the disclination charge of Kane-Mele model with the prescribed form of the Rashba term is unique. (However, other values of the flux can be considered by changing the detailed form of the Rashba term.) Consider an example where time-reversal symmetry is preserved and the two layers are spin-up and down of a spin-1/2 system, then $\eta = 0$ and $\Phi_0 = \pi/6$ per sector. Following these arguments, if one is given disclination charges of Haldane model in Table, then charges of Kane-Mele model can be derived using equation

$$\delta Q_{KM}^{\text{center}}(m) = 2[\delta Q_H^{\text{center}}(m) \mp m \frac{\pi/6}{2\pi}], \quad (4.13)$$

where the sign \mp depends on QSH phase $0 < \phi < \pi$ or $-\pi < \phi < 0$.

For the other type of disclination, where vertex of a hexagon is chosen as disclination center, one needs to use rotations through $2\pi/3$ and $t(\alpha + 2\pi/3) = U^2 t(\alpha) U^{-2}$, with U the same matrix as in Equation (4.12). The disclination charges are listed in Table 4.8. Similarly,

Table 4.8. Excess Charge of Kane-Mele model, vertex-type disclination, QSH phase $0 < \phi < \pi$.

Number of sectors m	1	2	3	4	5	κ
Total Curvature/ 2π	2/3	1/3	0	-1/3	-2/3	
$[\delta Q_{KM}^{\text{vertex}}]_{\text{frac}}$	2/3	1/3	0	2/3	1/3	-2

one can derive charges in Table from Table of the same disclination type of Haldane model. The relation is

$$\delta Q_{KM}^{\text{vertex}}(m) = 2[\delta Q_H^{\text{vertex}}(m) \mp m \frac{\pi/3}{2\pi}], \quad (4.14)$$

where the phase $\pi/6$ has been replaced with $\pi/3$.

4.3 Topological Gravitational Response – finding the GCC

The GCC κ calculated for topological lattice systems in this work will be generalized from Wen and Zee's effective theory of the gravitational response of Hall fluids on continuous curved spaces [53]. Wen and Zee discussed the continuum physics of Hall fluids in presence of

electromagnetic fields and small curvature variations in space using the effective Lagrangian [53]

$$\mathcal{L} = \frac{1}{4\pi}(aK\epsilon\partial a + 2At\epsilon\partial a + 2\omega s\epsilon\partial a) + aj. \quad (4.15)$$

The first term is a Chern-Simons self interaction for the internal gauge fields a ; the second and third term describe couplings of current to electromagnetic potential A and spatial connection, ω , respectively; the last term is coupling between gauge field to quasiparticle current j ; K and t are an integer-value matrix and vector characterizing the topological order of the system; s is the so-called spin vector which should not be confused with electronic spins. By the variational method one obtains the charge density or 0-component of electromagnetic current J^0 :

$$\rho(x) = \frac{1}{2\pi}[tK^{-1}t(\partial^1 A^2 - \partial^2 A^1) + tK^{-1}s(\partial^1 \omega^2 - \partial^2 \omega^1)] \equiv \frac{1}{2\pi}[\nu B + \kappa K_G(x)]. \quad (4.16)$$

The first term is proportional to magnetic flux density, $B = \partial^1 A^2 - \partial^2 A^1$, and the second term is proportional to the local Gaussian curvature $K_G(x) = \partial^1 \omega^2 - \partial^2 \omega^1$. κ is the so-called gravitational coupling constant (GCC), the excess charge density response with Gaussian curvature.

Integrating $\rho(x)$ over a closed manifold, Wen and Zee found

$$N_e = \nu N_\phi + 2\kappa(1 - g). \quad (4.17)$$

N_e and N_ϕ are the *integer* number of electrons and flux quanta over the area respectively. g , an *integer*, is the genus of the surface. ν is the filling factor, a *rational fraction*. This equation can only be satisfied if κ is a rational fraction. This indicates that the GCC is topologically quantized and this is the central reason motivating us to explore generalizations to a broader class of insulating states.

Thus, we will generalize the quantized curvature-induced charge response,

$$\rho(x) = \frac{\kappa K_G(x)}{2\pi}, \quad (4.18)$$

to other lattice topological states of matter. The case of quantum Hall states on the lattice has been studied in [54]. We will consider Chern insulators or time-reversal invariant topological insulators.

Before deriving an analogous equation for topological lattice systems, I will point out an important distinction between Hall fluids and Chern/topological insulators. Chern/topological insulators have no net magnetic field. Thus, their charge density on a flat lattice is a fixed amount per lattice site, as dictated by band theory. This is different in QH states, where the density is fixed by the magnetic flux density. A consequence is that vacancies can change the total charge near the disclination. These correspond to an integer in square and triangular lattices, and $1/2$ per occupied band on the honeycomb lattice.

Another consideration is that we have to consider the total accumulated charge at disclinations, not a charge density since the long-wavelength picture is no longer valid. Removing the non-universal corrections considered this far, the TGR equation looks like

$$[\delta Q]_{\text{frac}} = \left(\kappa \frac{K_G}{2\pi} \right)_{\text{frac}}, \quad (4.19)$$

where δQ is the net excess charge at the disclination, K_G is the total Gaussian curvature of the disclination (the Frank angle) and the fraction operation mods out the integer part (or $1/2$ for the Honeycomb lattice with odd number of occupied bands).

Our next consideration is the following: if the topological state carries Chern number C , when an effective magnetic flux is inserted through the disclination center, an excess charge will accumulate which can be calculated from Laughlin's argument. Therefore the charge at a disclination center, corrected for non-universal effects stemming from local bound states and vacancies, arise from two sources: the quantum Hall effect acting on fictitious magnetic fluxes and singular curvature of disclinations.

We next consider the source of this fictitious magnetic flux. As discussed while constructing tight-binding models, the U matrix associated with rotation symmetry has an undetermined phase η , which can only take a set of discrete values. η exerts a nontrivial

effect at disclinations, yielding an overall Aharonov-Bohm-like phase of $m\eta$ as a particle rotates around an m -fold disclination. Incorporating this,

$$[\delta Q]_{\text{frac}} = \left(\kappa \frac{K_G}{2\pi} + C \frac{m\eta}{2\pi} \right)_{\text{frac}}, \quad (4.20)$$

Since models with different η values are all topologically the same, we have to mod out its effect when calculating the GCC. For a lattice model without external magnetic field, fixing the rotation matrix U to satisfy either $U^n = 1$ or $U^n = -1$, η can only take value $2\pi k/n$, with k an integer going from 0 to $n-1$. Combining all these successive modular observations, I conclude that the value of $\text{mod}(\kappa, \text{g.c.d.}(n, C))$ is *universal* for a specific kind of lattice topological phase of matter. This is true for all calculations I have done so far.

4.4 Summary

I considered the charge response of a large class of quantum topological lattice states to real space curvature and implemented them onto disclinations. I first implemented a procedure for adapting any tight-binding models, defined in translation-invariant flat space, to disclinations on the lattice. I discovered fractional quantization of the disclination charge and discuss how to extract topological phase-specific universal behaviors from the data. Finally, a universal generalization of the Wen-Zee theory of gravitational response in continuum quantum Hall states was formulated, applicable to all lattice topological states of matter. I look forward to what this means for the general theory of topological invariants in quantum condensed matter physics.

5. GEOMETRIC RESPONSE OF QUANTUM HALL STATES TO ELECTRIC FIELDS

5.1 Introduction

Quantum Hall states are first examples of topological states of matter discovered to have quantized charge Hall conductance [1]–[5]. Less is known about any universal aspects of their response to nonuniform electric fields. Some recent developments, involving effective field theory formulations of quantum Hall physics in the continuum, have connected the gravitational coupling constant, in the guise of anomalous viscosity, to coefficients in the gradient expansion encapsulating local current density response to a nonuniform electric field [62]–[64]. This is a surprising observation, since it signifies a connection between the response of quantum Hall states to two very different kinds of perturbations – linear charge density response to real space curvature (the gravitational coupling constant is the response coefficient there) and current response to non-uniform fields.

Here, to elucidate this remarkable connection, we start from a novel geometric picture of quantum Hall wavefunctions and derive that nonuniform electric fields mimic the presence of spatial curvature [65]. We describe quantum Hall physics in terms of gauge-invariant variables (GIV), i.e. kinetic momentum and guiding center coordinates of electronic motion [66]. The two components belonging to each of these operators satisfy canonical commutation relations, similar to that between position and momentum in quantum mechanics, while these two sets of operators mutually commute and are independent. These pairs can therefore be chosen as coordinates of two independent dynamical phase spaces, allowing definitions of a new quantum basis for expressing the electronic wavefunctions.

Under the GIV formalism, we will first show how Landau quantization occurs and the extensive degeneracy of Landau levels can be calculated. We will then present calculations within this formalism which clearly show the shearing, shifting and drifting of cyclotron orbits in the presence of a nonuniform electric field. The nonuniform field gives rise to an effective metric, thus the charge density response should contain a part that arises from the physics of gravitational response and thus involves the gravitational constant! We present

analytic and numerical calculations which validate this reasoning in IQH states, neglecting spin effects.

5.2 Gauge Invariant Variables in Quantum Hall Physics

The kinetic momentum operator and guiding center coordinate operator for cyclotron motion of 2D electron gas in magnetic field are defined as [66]

$$\hat{\boldsymbol{\pi}} = \hat{\mathbf{p}} + e\mathbf{A}, \quad \hat{\mathbf{R}} = \mathbf{r} + \frac{l_B^2}{\hbar} \hat{z} \times \hat{\boldsymbol{\pi}}, \quad (5.1)$$

where \mathbf{A} is the vector potential of magnetic field, $l_B = \sqrt{\hbar/eB}$ is the magnetic length and magnetic field is assumed to be along z direction, $\mathbf{B} = B\hat{z}$. For brevity, we will set the magnetic length l_B , electric charge e and \hbar to be unity, then these operators satisfy commutation relation

$$[\hat{R}_x, \hat{R}_y] = i, \quad [\hat{\pi}_y, \hat{\pi}_x] = i, \quad [\hat{\pi}_i, \hat{R}_j] = 0 \quad (5.2)$$

These operators are found to be gauge invariant, since under a gauge transformation $\mathbf{A} \rightarrow \mathbf{A}^\omega = \mathbf{A} + \nabla\omega$, the position basis $\langle x, y | \rightarrow \langle x, y | e^{-i\omega}$, which implies the momentum operator undergoing a change $\hat{\mathbf{p}} \rightarrow \hat{\mathbf{p}} - \nabla\omega$, therefore $\hat{\boldsymbol{\pi}} = \hat{\mathbf{p}} + \mathbf{A}$ remains invariant.

Due to commutation relation (5.2), simultaneous eigenstates of a pair of operators $\{\hat{\pi}_i, \hat{R}_j\}$ can be found, which is denoted as $|\pi_i, R_j\rangle$. These states can be further written into basis of coordinates x, y . For instance, define the basis wave $\chi_{R_x, \pi_y}(x, y) \equiv \langle x, y | R_x, \pi_y \rangle$. $\chi_{R_x, \pi_y}(x, y)$ may assume different forms under different gauge choices. If one chooses the Landau gauge $\mathbf{A}^L = x\hat{y}$ (B has been set to 1), then it satisfies eigenvalue equations

$$\begin{aligned} \hat{R}_x \chi_{R_x, \pi_y}^L &= i\partial_y \chi_{R_x, \pi_y}^L = R_x \chi_{R_x, \pi_y}^L, \\ \hat{\pi}_y \chi_{R_x, \pi_y}^L &= (-i\partial_y + x) \chi_{R_x, \pi_y}^L = \pi_y \chi_{R_x, \pi_y}^L. \end{aligned} \quad (5.3)$$

The solution is found to be

$$\chi_{R_x, \pi_y}^L(x, y) = \delta(x - R_x - \pi_y) e^{-iR_x y}. \quad (5.4)$$

This set of basis wavefunctions satisfy orthogonality relation

$$\iint dxdy \chi_{R_x, \pi_y}^L(x, y)^* \chi_{R_x, \pi_y}^L(x, y) = \delta(R_x - R_x) \delta(\pi_y - \pi_y). \quad (5.5)$$

If alternatively one chooses the symmetric gauge $\mathbf{A}^S = (-y\hat{x} + x\hat{y})/2$, then the eigenvalue equaitons become

$$\begin{aligned} \hat{R}_x \chi_{R_x, \pi_y}^S &= (i\partial_y + \frac{x}{2}) \chi_{R_x, \pi_y}^S = R_x \chi_{R_x, \pi_y}^S, \\ \hat{\pi}_y \chi_{R_x, \pi_y}^S &= (-i\partial_x + \frac{y}{2}) \chi_{R_x, \pi_y}^S = \pi_y \chi_{R_x, \pi_y}^S \end{aligned} \quad (5.6)$$

whose solution is

$$\chi_{R_x, \pi_y}^S(x, y) = \delta(x - R_x - \pi_y) e^{-iR_x y} e^{i\frac{xy}{2}}. \quad (5.7)$$

Comparing (5.4) and (5.7) one can see the two basis waves are different by a factor $e^{ixy/2}$, which is as expected from the gauge transformation $\mathbf{A}^S = \mathbf{A}^L + \nabla(-xy/2)$. With the normalized basis wave $\chi(x, y)$ determined, a single-particle electronic wavefunction in representation of spatial coordinates x, y can be brought to R_x, π_y coordinates, using formula

$$\Psi(R_x, \pi_y) = \iint dxdy \chi^*(x, y) \Phi(x, y). \quad (5.8)$$

Within the GIV formalism, let us consider the Hamiltonian of 2D electrons in a purely magnetic field:

$$\hat{\mathcal{H}} = K(\hat{\mathbf{p}} + \mathbf{A}) = K(\hat{\boldsymbol{\pi}}) = \frac{\hat{\boldsymbol{\pi}}^2}{2}, \quad (5.9)$$

where the kinetic energy K is assumed to be quadratic in kinetic momentum $\hat{\boldsymbol{\pi}}$. Then variables R_x, π_y of the wavefunction are separable, $\Psi(R_x, \pi_y) = \psi(R_x)\eta(\pi_y)$. Here $\psi(R_x)$ is an arbitrary square-integrable function and $\eta(\pi_y)$ satisfies equation of simple harmonic oscillator. An energy eigenstate is found to be

$$\Psi_n(R_x, \pi_y) = \psi(R_x)\eta_n(\pi_y), \quad n = 0, 1, \dots \quad (5.10)$$

with energy eigenvalue $\varepsilon_n = n + 1/2$ and η_n the n th harmonic oscillator. Solution (5.10) shows that the Landau levels structure of 2D electron gas is featured by η_n and the extensive degeneracy of each level is given by degree of freedom of the arbitrary function $\psi(R_x)$.

Function $\psi(R_x)$ can be expanded with different basis. For example, one can consider the set of eigenstates of operator $\hat{\mathbf{R}}^2 = \hat{R}_x^2 + \hat{R}_y^2$ since it is another harmonic oscillator whose eigenstates form a complete orthogonal basis of the one-dimensional Hilbert space. The eigenstates are $\eta_m(R_x)$, $m = 0, 1, \dots$ with eigenvalue $2m + 1$. Therefore an energy eigenstate can be cast as

$$\Psi_{m,n}(R_x, \boldsymbol{\pi}_y) = \eta_m(R_x) \eta_n(\boldsymbol{\pi}_y), \quad m, n = 0, 1, \dots \quad (5.11)$$

Transforming back to x, y coordinate representation using the basis wave of symmetric gauge, χ_{R_x, π_y}^S , one obtains

$$\begin{aligned} \tilde{\Psi}_{m,n}(x, y) &= \iint dR_x d\boldsymbol{\pi}_y \chi_{R_x, \pi_y}^S(x, y) \Psi_{mn}(R_x, \boldsymbol{\pi}_y) \\ &\propto e^{i\frac{xy}{2}} e^{-\frac{x^2+y^2}{4}} (x + iy)^{\frac{|m-n|-(m-n)}{2}} (x - iy)^{\frac{|m-n|+(m-n)}{2}} L_{n+m-|m-n|}^{|m-n|} \left(\frac{x^2 + y^2}{2} \right), \end{aligned} \quad (5.12)$$

Here L_n^m is the associated Legendre polynomials. The wavefunction (5.12) differs from the energy eigenstate in symmetric gauge [67] by a phase factor $e^{i\frac{xy}{2}}$.

5.3 Response to Nonuniform Electric Field: Analytical Result

Considering the situation where a nonuniform electric field is present. The Hamiltonian becomes

$$\hat{\mathcal{H}} = K(\hat{\mathbf{p}} + \mathbf{A}) - V(\mathbf{r}) = \frac{\hat{\boldsymbol{\pi}}^2}{2} - V(\hat{\mathbf{R}} + \hat{\boldsymbol{\pi}} \times \hat{\mathbf{z}}), \quad (5.13)$$

where V is potential energy due to electric field, with a minus sign accounting for negative charge of electrons. Our target is to calculate the local charge and current density operators in terms of gradient expansions of the electric potential: V . We assume the change of V is slow in space such that its variation in a magnetic length is much smaller than gap between

Landau levels. Since magnetic length l and energy gap $\hbar\omega_c$ have been set equal to 1, the slowly varying condition is equivalent to following

$$\partial_{\mathbf{r}}^m V(\mathbf{r}) \ll 1, \quad m = 1, 2, \dots \quad (5.14)$$

This condition on V can be used to approximate operator $V(\hat{\mathbf{R}} + \hat{\boldsymbol{\pi}} \times \hat{\mathbf{z}})$ by the first few terms of Taylor series:

$$V(\hat{\mathbf{R}} + \hat{\boldsymbol{\pi}} \times \hat{\mathbf{z}}) = V(\hat{\mathbf{R}}) + \partial_a V(\hat{\mathbf{R}}) \epsilon_{ap} \hat{\pi}_p + \frac{1}{2} \partial_{ab}^2 V(\hat{\mathbf{R}}) \epsilon_{ap} \epsilon_{bq} \hat{\pi}_p \hat{\pi}_q + \frac{1}{6} \partial_{abc}^3 V(\hat{\mathbf{R}}) \epsilon_{ap} \epsilon_{bq} \epsilon_{cr} \hat{\pi}_p \hat{\pi}_q \hat{\pi}_r + \dots \quad (5.15)$$

where the summations over repeated indices have been omitted, and ϵ is Levi-Civita tensor in two dimensions. Here only the perturbative terms up to 3rd order of kinetic momentum $\hat{\boldsymbol{\pi}}$ are written out explicitly, since we will show this approximation can be simplified to a quadratic polynomial of \hat{R} and $\hat{\boldsymbol{\pi}}$.

The simplest case is to ignore all perturbative terms, i.e., $V(\mathbf{r}) \approx V(\hat{\mathbf{R}})$. Since $[\hat{\mathbf{R}}, \hat{\boldsymbol{\pi}}] = 0$, variables of eigenstates of Hamiltonian (5.13) are still separable. An energy eigenstate has the form

$$\Psi_{m,n}(R_x, \boldsymbol{\pi}_y) = \psi_m(R_x) \eta_n(\boldsymbol{\pi}_y), \quad (5.16)$$

where η_n is still the n th harmonic oscillator, and ψ_m is an eigenstate of operator $V(\hat{\mathbf{R}})$:

$$V(\hat{\mathbf{R}}) \psi_m = -v_m \psi_m. \quad (5.17)$$

The energy eigenvalue of state $\Psi_{m,n}$ is the Landau level energy ε_n modified by electric potential energy v_m ,

$$E_{m,n} = \varepsilon_n + v_m. \quad (5.18)$$

Next, to take the higher order perturbations into account, for a general treatment, one can use Wick contraction to reduce each term to degree 1 or 2 of the kinetic momentum. In

the expansion (5.15) which is up to $\hat{\pi}^3$, only the cubic term is affected. For instance, as a perturbation to n th Landau level, Wick contraction gives

$$\hat{\pi}_p \hat{\pi}_q \hat{\pi}_r \approx \langle \hat{\pi}_q \hat{\pi}_r \rangle_n \hat{\pi}_p + \langle \hat{\pi}_p \hat{\pi}_r \rangle_n \hat{\pi}_q + \langle \hat{\pi}_p \hat{\pi}_q \rangle_n \hat{\pi}_r = \varepsilon_n (\delta_{qr} \hat{\pi}_p + \delta_{pr} \hat{\pi}_q + \delta_{pq} \hat{\pi}_r), \quad (5.19)$$

where $\langle \rangle_n$ means the average under n th Landau level wavefunction $\eta_n(\pi_y)$, and $\varepsilon_n = n + \frac{1}{2}$ is the Landau level energy. As a result, the effective Hamiltonian for n th Landau level perturbed up to 3rd order of $\hat{\pi}$ is:

$$\begin{aligned} \hat{\mathcal{H}}^{(n)} &\approx \frac{\hat{\pi}^2}{2} - V(\hat{\mathbf{R}}) - \partial_a V(\hat{\mathbf{R}}) \epsilon_{ap} \hat{\pi}_p - \frac{1}{2} \partial_{ab}^2 V(\hat{\mathbf{R}}) \epsilon_{ap} \epsilon_{bq} \hat{\pi}_p \hat{\pi}_q - \frac{\varepsilon_n}{2} \partial_{acc}^3 V(\hat{\mathbf{R}}) \epsilon_{ar} \hat{\pi}_r \\ &= \frac{\hat{\pi}^2}{2} - V(\hat{\mathbf{R}}) + \left[E_a(\hat{\mathbf{R}}) + \frac{\varepsilon_n}{2} \partial_a \nabla \cdot \mathbf{E}(\hat{\mathbf{R}}) \right] \epsilon_{ap} \hat{\pi}_p + \frac{1}{2} \left[\delta_{ab} \nabla \cdot \mathbf{E}(\hat{\mathbf{R}}) - \partial_a E_b(\hat{\mathbf{R}}) \right] \hat{\pi}_a \hat{\pi}_b. \end{aligned} \quad (5.20)$$

where $\mathbf{E}(\hat{\mathbf{R}}) = -\nabla V(\hat{\mathbf{R}})$ has been used.

The quadratic expression (5.20) enables one to extract a metric form of the perturbed Hamiltonian,

$$\hat{\mathcal{H}}^{(n)} = \frac{1}{2} g_{ab} (\hat{\pi}_a - \Delta_a) (\hat{\pi}_b - \Delta_b) - V(\hat{\mathbf{R}}), \quad (5.21)$$

where g_{ab}, Δ_a are the induced metric tensor and kinetic momentum shift by the nonuniform electric field, which can be explicitly written in terms of \mathbf{E} and its derivatives. This Hamiltonian can be further simplified to a modified simple harmonic oscillator form:

$$\hat{\mathcal{H}}^{(n)} = \frac{1}{2} \omega(\hat{\mathbf{X}}) \hat{\Pi}^2 - V(\hat{\mathbf{X}}), \quad (5.22)$$

where $\hat{\mathbf{X}}, \hat{\Pi}$ are the modified guiding center coordinates and kinetic momentum operator, respectively; $\omega(\hat{\mathbf{X}})$ is the modified gap between Landau levels. To obtain $\hat{\mathbf{X}}$ and $\hat{\Pi}$, one can decompose the metric tensor matrix as $g = \sqrt{\det(g)} (\Lambda^{-1})^T \Lambda^{-1}$ where Λ is a unimodular

matrix related to shearing and rotation of electron orbitals. In terms of the shifting Δ and shearing Λ ,

$$\begin{aligned}\hat{X}_a &= \hat{R}_a + (\partial_p \Delta_a) \hat{\pi}_p - \frac{1}{2} \epsilon_{ar} \epsilon_{ps} (\partial_r \Lambda_{sq}) \hat{\pi}_p \hat{\pi}_q, \\ \hat{\Pi}_a &= (\Lambda^{-1})_{ab} (\hat{\pi}_b - \Delta_b),\end{aligned}\tag{5.23}$$

and they are found to satisfy the same commutation relation as $\hat{\mathbf{R}}$ and $\hat{\boldsymbol{\pi}}$ to lowest-order approximation. Since $\langle \hat{\boldsymbol{\Pi}} \rangle = 0$, $\langle \hat{\boldsymbol{\pi}} \rangle = \boldsymbol{\delta}(\mathbf{R})$ showing that the orbit drifts with velocity $\mathbf{v}_d = \boldsymbol{\delta}(\mathbf{R})$. The preceding analysis yields a physical picture of how the cyclotron orbit is shifted and sheared by the nonuniform electric field, and drifts in a direction that is perpendicular to the electric field. This picture is summarized in Figure 5.1.

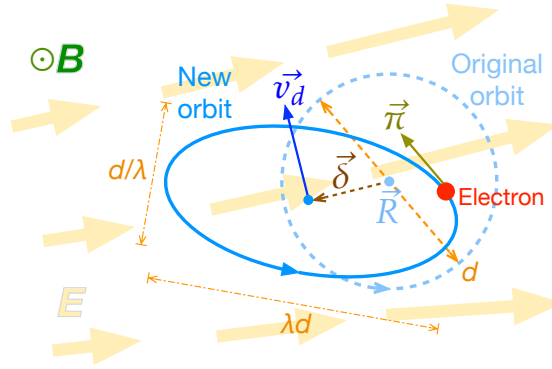


Figure 5.1. A geometric summary of how a non-uniform electric field, \mathbf{E} , deforms a cyclotron orbit. The changes can be expressed in terms of a vector field, $\Delta(\mathbf{R})$, and a shearing field, $\Lambda(\mathbf{R})$. The new orbit is shifted by amount $\boldsymbol{\delta}(\mathbf{R}) = \hat{\mathbf{z}} \times \Delta(\mathbf{R})$ with respect to the original center, \mathbf{R} , and acquires a drift velocity, $\mathbf{v}_d = \Delta(\mathbf{R})$. The orbit is also sheared into an ellipse with aspect ratio λ^2 , where λ and $1/\lambda$ are the eigenvalues of $\Lambda(\mathbf{R})$. The guiding center coordinate, \mathbf{R} , labels the field-free orbit center while the kinetic momentum, $\boldsymbol{\pi}$, gives the velocity of the electron. This figure has been reproduced from our publication [65].

In terms of the modified Hamiltonian (5.22), one can make a further assumption of Landau level projection that in its eigenstate wavefunctions the variables $\hat{\mathbf{X}}$ and $\hat{\boldsymbol{\Pi}}$ are separable, $W_{m,n}(\mathbf{X}, \boldsymbol{\Pi}) = \mathcal{W}_m(\mathbf{X})w_n(\boldsymbol{\Pi})$, where n is the Landau level index and m labels

different perturbed states in the level. These wavefunctions are related to $\Psi_{m,n}(R_x, \boldsymbol{\pi}_y)$ through Wigner pseudoprobability distribution [68].

To calculate the local charge and current densities of n th Landau level, one needs to evaluate the average of operators:

$$\begin{aligned}\hat{\rho}(\mathbf{x}) &= -\delta^2(\hat{\mathbf{r}} - \mathbf{x}), \\ \hat{\mathbf{j}}(\mathbf{x}) &= -\frac{1}{2}\{\hat{\boldsymbol{\pi}}, \delta^2(\hat{\mathbf{r}} - \mathbf{x})\},\end{aligned}\tag{5.24}$$

for a single particle state $W_{m,n}$ and sum over all states in the same Landau level:

$$\begin{aligned}\rho^{(n)}(\mathbf{x}) &= -\sum_m \iint d^2X d^2\Pi W_{m,n}(\mathbf{X}, \boldsymbol{\Pi}) \delta^2(\mathbf{r} - \mathbf{x}), \\ \mathbf{j}_a^{(n)}(\mathbf{x}) &= -\sum_m \iint d^2X d^2\Pi W_{m,n}(\mathbf{X}, \boldsymbol{\Pi}) \pi_a \delta^2(\mathbf{r} - \mathbf{x}).\end{aligned}\tag{5.25}$$

They are found to have contributions from the drifting and shearing of cyclotron orbitals separately. Using $\rho_0 = -1/2\pi$ to denote the charge density for each Landau level in absence of electric field, the charge and current responses are:

$$\begin{aligned}\left[\frac{\rho^{(n)}(\mathbf{x}) - \rho_0}{\rho_0}\right]_{\Delta} &= \nabla \cdot \mathbf{E}(\mathbf{x}) + \varepsilon_n \nabla^2(\nabla \cdot \mathbf{E}), \\ \left[\frac{\rho^{(n)}(\mathbf{x}) - \rho_0}{\rho_0}\right]_{\Lambda} &= -\frac{\varepsilon_n}{4} \nabla^2(\nabla \cdot \mathbf{E}); \\ [\mathbf{j}_a^{(n)}(\mathbf{x})]_{\Delta} &= -\frac{\epsilon_{ab}}{2\pi} [\mathbf{E} + 2\varepsilon_n \nabla(\nabla \cdot \mathbf{E})]_b, \\ [\mathbf{j}_a^{(n)}(\mathbf{x})]_{\Lambda} &= \frac{\epsilon_{ab} \varepsilon_n}{2\pi} [\nabla(\nabla \cdot \mathbf{E})]_b.\end{aligned}\tag{5.26}$$

In the charge response above, $[\delta\rho^{(n)}/\rho_0]_{\Delta}$ can be interpreted as charge polarization due to shifting of orbitals centers, while the shearing contribution $[\delta\rho^{(n)}/\rho_0]_{\Lambda}$ can be shown as equivalent to the gravitational response. It is known from Wen and Zee's shift theory of quantum Hall fluid [53] that local spatial curvature can induce an extra charge density for a filled Landau level. The induced charge is proportional to Gaussian curvature through gravitational coupling constant κ . κ is believed to be a topological invariant, and for n th

($n = 0, 1, \dots$) Landau level, it happens to coincide with the Landau level spectrum, $\kappa^{(n)} = n + 1/2$.

According to my analysis, the nonuniform electric field induces an effective metric of space, so using Brioschi formula [69], a local Gaussian curvature can be extracted from the shearing matrix Λ :

$$K_G(\mathbf{R}) = -\frac{1}{4}\nabla^2(\nabla_{\mathbf{R}} \cdot \mathbf{E}(\mathbf{R})). \quad (5.27)$$

Therefore the gravitational response of charge density is

$$\delta\rho_G^{(n)}(\mathbf{x}) = -\frac{\kappa^{(n)}}{2\pi}K_G(\mathbf{x}) = -\rho_0\frac{\varepsilon_n}{4}\nabla^2(\nabla \cdot \mathbf{E}), \quad (5.28)$$

which agrees with the shearing contribution $[\delta\rho^{(n)}/\rho_0]_{\Lambda}$ in (5.26).

5.4 Response to Nonuniform Electric Field: Numerical Result

I use the Hofstadter model to numerically study the response of quantum Hall states to nonuniform electric fields. The Hofstadter model is a nearest-neighbor tight-binding model of spinless electrons propagating on the square lattice in the presence of a uniform magnetic field [70]. The magnetic field is incorporated into the tight-binding hopping amplitudes by the Peierls substitution method [71]. Assuming isotropic hoppings along x, y direction and choosing the Landau gauge, $\mathbf{A} = (0, Bx)$, the Hamiltonian of Hofstadter model is:

$$\hat{\mathcal{H}}_0 = -\sum_{m=1}^{L_x}\sum_{n=1}^{L_y}t(\hat{c}_{m+1,n}^\dagger\hat{c}_{m,n} + e^{i2\pi m\phi}\hat{c}_{m,n+1}^\dagger\hat{c}_{m,n}) + h.c.. \quad (5.29)$$

Here L_x, L_y are the lengths of the lattice along the x, y directions respectively, in units of the lattice constant a ; t is the isotropic hopping amplitude; ϕ is the number of flux quanta per unit cell and related to B through $\phi h/e = Ba^2$. When $\phi = p/q$ with p, q coprime, the translational symmetry of square lattice is partially broken (cf. when ϕ is irrational, then translational symmetry along x direction is totally broken), such that the total translation group shrinks to a subgroup called magnetic translation group [72]–[74] and a Bloch-like band

structure can be derived. Hofstadter discovered that the energy spectrum versus (rational) ϕ is an elegant fractal, the Hofstadter butterfly [70] (Figure 5.2).

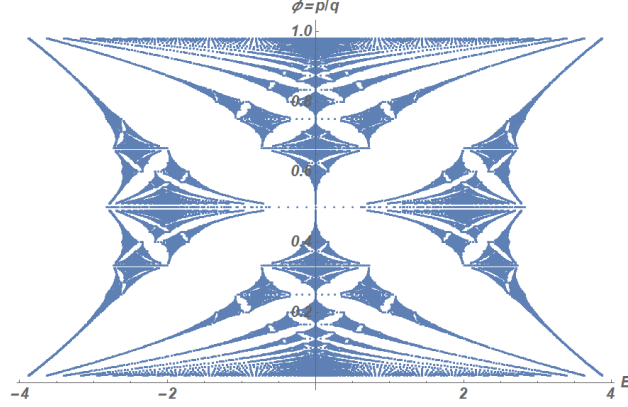


Figure 5.2. Plot of the Hofstadter butterfly. Energy eigenvalues of the Hofstadter model versus flux quanta per unit cell, ϕ . We consider only rational values for the flux, $\phi = p/q$, so as to be able to impose periodic boundary conditions. Because of periodicity of spectrum with ϕ , it suffices to consider only $0 < \phi < 1$. The length L_x must be an integer multiple of q . For each $\phi = p/q$, I have chosen the square lattice to have dimensions $L_y = 20$ and L_x the largest multiple of q not exceeding 100. t and a have been set to 1.

The strong field limit of Hofstadter model, $0 \ll \phi \ll 1$, can be understood from perturbation theory [8]. In this limit, the energy spectrum consists of a handful of subbands with their bandwidths being comparable to the inter-band energy gaps. Here we focus on the weak field limit, $\phi \rightarrow 0$, and low energy, $E \rightarrow 0$ since we wish to reproduce the physics of continuum Landau levels.

The nearest neighbor tight-binding model on the square lattice, without magnetic field, yields the band dispersions:

$$\varepsilon_{\mathbf{k}\pm} = \pm 2t [\cos(k_x a) + \cos(k_y a)], \quad (5.30)$$

where a is the lattice constant. The effective mass of the electron in the continuum limit, $k \rightarrow 0$, can be obtained by Taylor-expanding of the band dispersion near the bottom of the band, i.e., about $k = 0$:

$$\varepsilon_{\mathbf{k},-} \approx -4t + ta^2(k_x^2 + k_y^2). \quad (5.31)$$

Comparing with the free electron dispersion, the effective mass is found to be $m^* = \hbar^2/2ta^2$. Recalling that the magnetic flux through a unit cell is $Ba^2 = \phi h/e$, one obtains the effective cyclotron frequency and magnetic length as

$$\omega_c^* = \frac{4\pi t\phi}{\hbar}, \quad l_B^* = \frac{a}{\sqrt{2\pi\phi}}. \quad (5.32)$$

To model electrons in a magnetic field in the continuum, the magnetic length needs to be much larger than lattice constant (but smaller than dimension of lattice) such that discrete details of the lattice are invisible. This condition, $a \ll l_B^* \ll L_x a, L_y a$, leads to the following constraint on choosing simulation parameters:

$$\frac{1}{L_x^2}, \frac{1}{L_y^2} \ll \phi \ll 1. \quad (5.33)$$

Figure 5.3 shows good match between continuum calculations and the low energy spectrum of the Hofstadter model with $|\phi| \ll 1$.

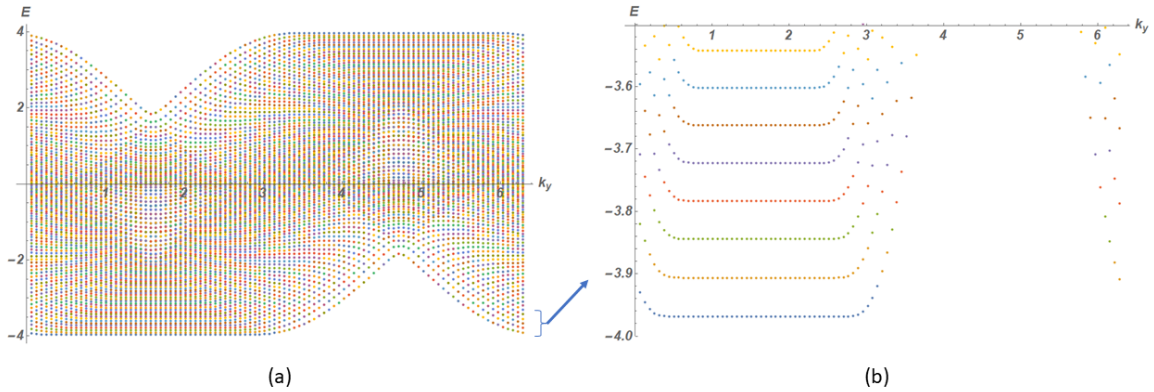


Figure 5.3. Disturbed Landau levels of Hofstadter model in the weak field limit. $t = 1$, $L_x = L_y = 100$, $\phi = 1/200$. (a) Energy dispersion with respect to k_y . In the Landau gauge chosen, translation symmetry along x direction is broken but along y direction is not, so k_y is a quantum number. (b) Inset plot of (a) in energy range $-4 \sim -3.5$. Gap between Landau levels is estimated to be $4\pi t\phi \approx 0.063$ which agrees with the calculation result. This figure has been reproduced from our publication [65].

Next, I turn on the nonuniform electric field. The electric field in lattice can be modeled by an on-site potential energy that varies from site to site. I will consider sinusoidal potential profiles corresponding to a single wavelength allowing us to directly obtain the k -dependent Fourier transforms of the response functions (see below). The electrostatic term in the Hamiltonian is:

$$\hat{\mathcal{H}}_1 = \sum_{m=1}^{L_x} \sum_{n=1}^{L_y} V_0 \sin \frac{2\pi m}{\lambda} \hat{c}_{m,n}^\dagger \hat{c}_{m,n}, \quad (5.34)$$

where λ is the wavelength of electric field in units of a . I will choose λ to be commensurate with L_x so as to be able to use periodic boundary conditions.

From linear response theory, the charge density response $\delta\rho(x)$ is related to electric potential $V(x)$ through the formula:

$$\frac{\delta\rho(x)}{\rho_0} = \int V(x') K(x - x') dx', \quad (5.35)$$

where $K(x - x')$ is the kernel of response and no y -dependence has been assumed. By doing a Fourier transform, the above equation leads to $\delta\rho(k)/\rho_0 = V(k)K(k)$. Since the electric potential is a single-frequency mode, $V(x) = V_0 \sin(2\pi x/\lambda)$, the charge response will be of the form $\delta\rho(x)/\rho_0 = A(\lambda) \sin(2\pi x/\lambda + \varphi)$, whence one can find the corresponding value of the Fourier-transformed response function: $K(k = 2\pi/\lambda) = A(\lambda)/V_0$.

In order to compare our numerical results with analytical calculations, it is easier to consider a sequence of N filled Landau levels. The total local charge density at x is then just the sum of the modulus-squared amplitudes of all occupied states, evaluated at x . The analytical result (5.26) yields:

$$\frac{\delta\rho^{(n)}}{\rho_0} = \nabla \cdot \mathbf{E}(\mathbf{x}) + \frac{3\varepsilon_n}{4} \nabla^2 (\nabla \cdot \mathbf{E}). \quad (5.36)$$

This, when summed over N lowest Landau levels, in turn yields the total excess charge to be

$$\frac{\delta\rho(x)}{\rho_{0,\text{tot}}} = \frac{1}{N} \sum_{n=0}^{N-1} \frac{\delta\rho^{(n)}}{\rho_0} = \nabla \cdot \mathbf{E}(\mathbf{x}) + \frac{3N}{8} \nabla^2 (\nabla \cdot \mathbf{E}), \quad (5.37)$$

where $\rho_{0,\text{tot}} = N\rho_0$ is the total charge density in the absence of an electric field. Reintroducing units and considering the x -dependent electric potential $V(x) = V_0 \sin(kx)$, corresponding to $k = 2\pi/\lambda$ and an electric field $\mathbf{E} = -\nabla V$, the theoretical prediction for charge response of Hofstadter model is:

$$\frac{\delta\rho(x)}{\rho_{0,\text{tot}}} = [(kl_B^*)^2 - \frac{3N}{8}(kl_B^*)^4] \frac{V(x)}{4\pi t\phi}. \quad (5.38)$$

The left side can be measured in our numerical experiments for various values of k , ϕ , N and V_0 , and compared to the expression on the right. Similar expressions can be derived for the local orbit energy and the current density. Comparisons between the theoretical predictions and numerical results, for the charge density, current density and local cyclotron energy are provided in Figures 5.4, 5.5 and 5.6 respectively. Evidently, there is an excellent match between numerical data and analytic theory.

5.5 Summary and Future Work

In this work a Hilbert space representation based on gauge-invariant variables (GIV) was provided to describe the quantum mechanics of 2D electrons in the presence of uniform magnetic fields. A nonuniform electric field was included as background and interactions between electrons were ignored. The case with interactions has been discussed elsewhere [75].

Using the GIV formalism, we derived a geometric picture of response of electron cyclotron orbitals to the nonuniform electric field. To recapitulate, the orbits get shifted from their original position and sheared. These modifications are characterized by the shift vector field Δ and shearing metric g , respectively. We then combined this geometric picture with the Wigner quasiprobability formalism to calculate linear responses of charge and current density to nonuniform electric fields and derived insights into how the gravitational coupling constant can be related to shearing of cyclotron orbits due to nonuniform electric field. A new result was obtained– the gravitational coupling constant appears in the charge density response to nonuniform electric fields.

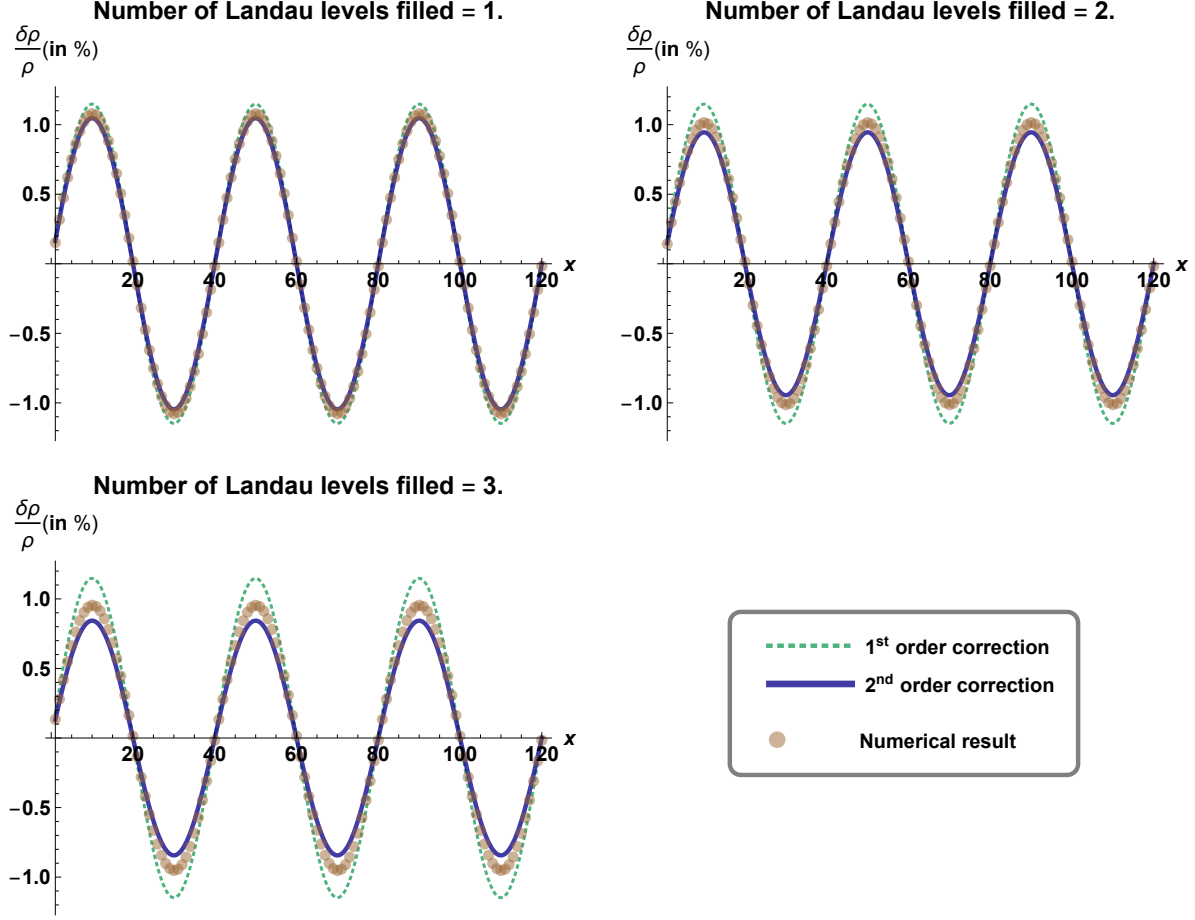


Figure 5.4. The spatial variation of local fractional charge density modulation in a nonuniform (sinusoidal) electric field. The Landau levels are modeled by the lowest bands in a Hofstadter model on a square lattice. The nonuniform electric field is generated by a sinusoidal background potential, which is small compared to the inter-Landau-level energy gap so that the system is in the linear response regime. The brown circles correspond to the local charge density values obtained via numerical diagonalization. The dashed green curve is the response obtained correct to the second derivative in the electric field, corresponding to the nonuniform polarization induced by cyclotron orbit shifts. The thick blue curve corresponds to our analytical results, correct to the third order in the derivatives of the electric field. For these plots, $V_0/e_c = 0.05$, $kl_B^* = 0.49$. This figure has been reproduced from our publication [65].

Numerical calculations on Hofstadter model in the weak field limit confirm our analytical results. Future directions may include investigating if the gravitational coupling constant continues to appear in the charge density response to nonuniform electric fields in interacting quantum Hall states, say in the Laughlin states, or to even wider classes of topological

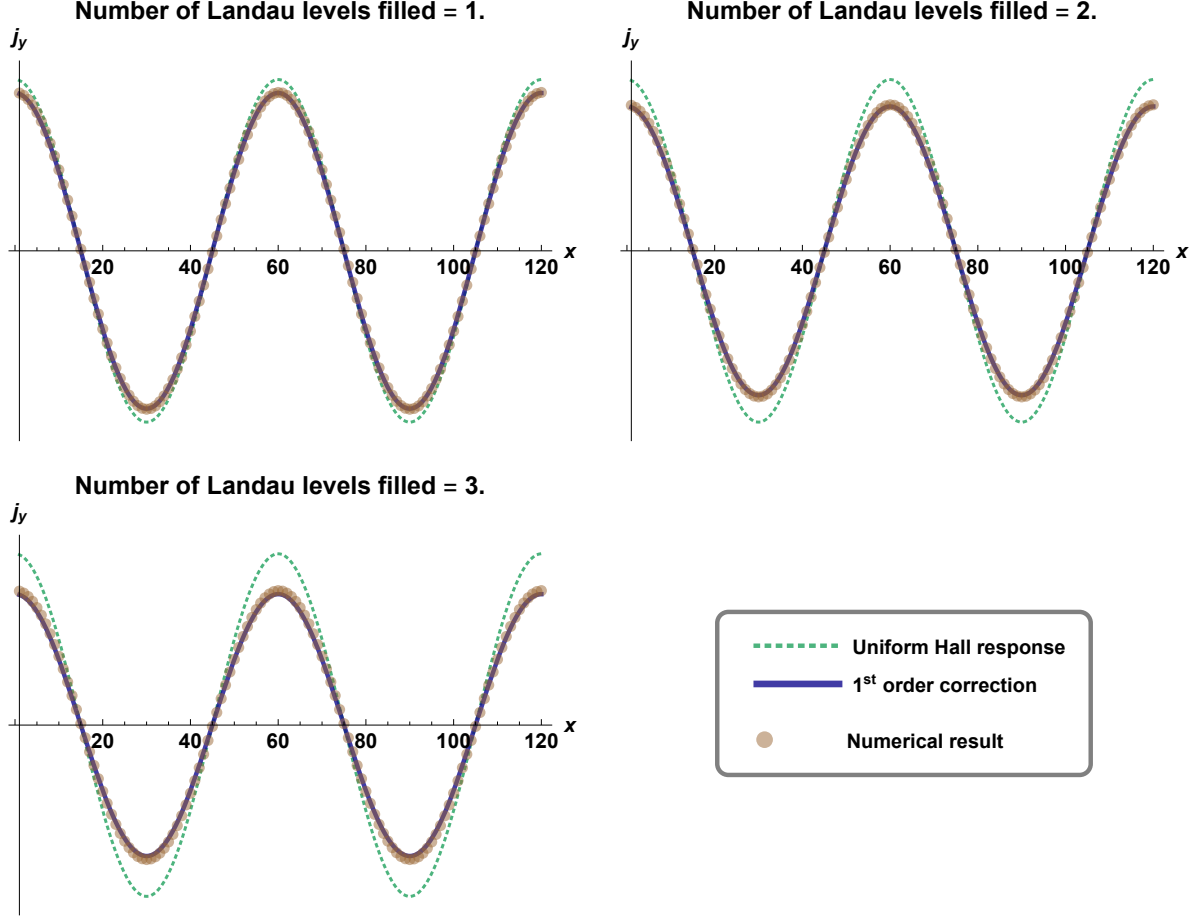


Figure 5.5. The spatial variation of local current density in a nonuniform (sinusoidal) electric field. The Landau levels are modeled by the lowest bands in a Hofstadter model on a square lattice. The nonuniform electric field is generated by a sinusoidal background potential, which is small compared to the inter-Landau-level energy gap so that the system is in the linear response regime. The brown circles correspond to the local current density values obtained via numerical diagonalization. The dashed green curve is the quantized local Hall response, which is correct when the electric field is uniform. The thick blue curve corresponds to our analytical results, correct up to the second order in the derivatives of the electric field. For these plots, $V_0/e_c = 0.05$, $kl_B^* = 0.32$. This figure has been reproduced from our publication [65].

materials. If our result holds generally, it will have implications for improving current formulations of the universal effective theory of quantum Hall states [64] and other topological band insulators.

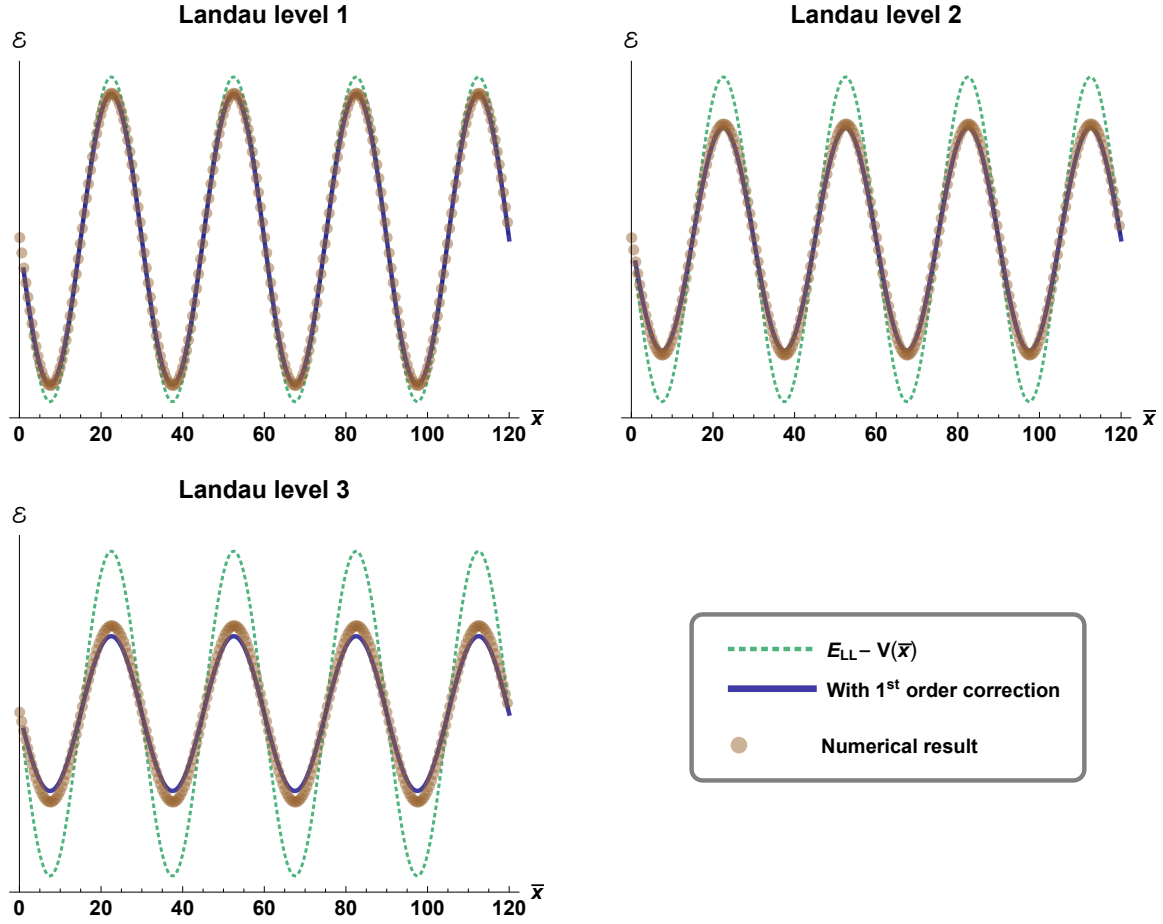


Figure 5.6. The variation of cyclotron orbit energy with orbit location, \bar{x} . The Landau levels are modeled by the lowest bands in a Hofstadter model on a square lattice. The nonuniform electric field is generated by a sinusoidal background potential, which is small compared to the inter-Landau-level energy gap, so that the system is in the linear response regime. The brown circles correspond to the cyclotron energies obtained via numerical diagonalization. The dashed green curve is the sum of the Landau level energy and the local potential energy, which is the correct energy when the electric field is uniform. The thick blue curve corresponds to our analytical results, correct up to the second order in the derivatives of the electric field. For these plots, $V_0/e_c = 0.05$, $kl_B^* = 0.65$. This figure has been reproduced from our publication [65].

5.6 Chapter Acknowledgements

The content of this chapter has been published and appears in: “Geometric response of quantum Hall states to electric fields”, Phys. Rev. B **103**, 155303 (2021) [65].

REFERENCES

- [1] K. v. Klitzing, G. Dorda, and M. Pepper, “New method for high-accuracy determination of the fine-structure constant based on quantized hall resistance,” *Physical review letters*, vol. 45, no. 6, p. 494, 1980.
- [2] R. B. Laughlin, “Quantized hall conductivity in two dimensions,” *Physical Review B*, vol. 23, no. 10, p. 5632, 1981.
- [3] B. I. Halperin, “Quantized hall conductance, current-carrying edge states, and the existence of extended states in a two-dimensional disordered potential,” *Physical Review B*, vol. 25, no. 4, p. 2185, 1982.
- [4] P. Streda, “Theory of quantised hall conductivity in two dimensions,” *Journal of Physics C: Solid State Physics*, vol. 15, no. 22, p. L717, 1982.
- [5] P. Streda, “Quantised hall effect in a two-dimensional periodic potential,” *Journal of Physics C: Solid State Physics*, vol. 15, no. 36, p. L1299, 1982.
- [6] D. C. Tsui, H. L. Stormer, and A. C. Gossard, “Two-dimensional magnetotransport in the extreme quantum limit,” *Physical Review Letters*, vol. 48, no. 22, p. 1559, 1982.
- [7] H. L. Stormer, D. C. Tsui, and A. C. Gossard, “The fractional quantum hall effect,” *Reviews of Modern Physics*, vol. 71, no. 2, S298, 1999.
- [8] D. J. Thouless, M. Kohmoto, M. P. Nightingale, and M. den Nijs, “Quantized hall conductance in a two-dimensional periodic potential,” *Physical review letters*, vol. 49, no. 6, p. 405, 1982.
- [9] F. D. M. Haldane, “Model for a quantum hall effect without landau levels: Condensed-matter realization of the” parity anomaly”,” *Physical review letters*, vol. 61, no. 18, p. 2015, 1988.
- [10] C. L. Kane and E. J. Mele, “Quantum spin hall effect in graphene,” *Physical review letters*, vol. 95, no. 22, p. 226 801, 2005.
- [11] C. L. Kane and E. J. Mele, “Z 2 topological order and the quantum spin hall effect,” *Physical review letters*, vol. 95, no. 14, p. 146 802, 2005.
- [12] X.-L. Qi, Y.-S. Wu, and S.-C. Zhang, “Topological quantization of the spin hall effect in two-dimensional paramagnetic semiconductors,” *Physical Review B*, vol. 74, no. 8, p. 085 308, 2006.

- [13] X.-L. Qi, Y.-S. Wu, and S.-C. Zhang, “General theorem relating the bulk topological number to edge states in two-dimensional insulators,” *Physical Review B*, vol. 74, no. 4, p. 045 125, 2006.
- [14] R. S. Mong and V. Shivamoggi, “Edge states and the bulk-boundary correspondence in dirac hamiltonians,” *Physical Review B*, vol. 83, no. 12, p. 125 109, 2011.
- [15] S. Murakami, S. Iso, Y. Avishai, M. Onoda, and N. Nagaosa, “Tuning phase transition between quantum spin hall and ordinary insulating phases,” *Physical Review B*, vol. 76, no. 20, p. 205 304, 2007.
- [16] M. König, H. Buhmann, L. W. Molenkamp, T. Hughes, C.-X. Liu, X.-L. Qi, and S.-C. Zhang, “The quantum spin hall effect: Theory and experiment,” *Journal of the Physical Society of Japan*, vol. 77, no. 3, p. 031 007, 2008.
- [17] W.-Y. Shan, H.-Z. Lu, and S.-Q. Shen, “Effective continuous model for surface states and thin films of three-dimensional topological insulators,” *New Journal of Physics*, vol. 12, no. 4, p. 043 048, 2010.
- [18] Z. B. Siu, S. G. Tan, and M. B. Jalil, “Effective hamiltonian for surface states of topological insulator nanotubes,” *Scientific reports*, vol. 7, no. 1, pp. 1–12, 2017.
- [19] R. Jackiw, “Fractional charge and zero modes for planar systems in a magnetic field,” *Physical Review D*, vol. 29, no. 10, p. 2375, 1984.
- [20] S.-Q. Shen, *Topological insulators*. Springer, 2012, vol. 174.
- [21] B. A. Bernevig, T. L. Hughes, and S.-C. Zhang, “Quantum spin hall effect and topological phase transition in hgte quantum wells,” *science*, vol. 314, no. 5806, pp. 1757–1761, 2006.
- [22] S.-Q. Shen, W.-Y. Shan, and H.-Z. Lu, “Topological insulator and the dirac equation,” in *Spin*, World Scientific, vol. 1, 2011, pp. 33–44.
- [23] P. A. M. Dirac, “The quantum theory of the electron,” *Proceedings of the Royal Society of London. Series A, Containing Papers of a Mathematical and Physical Character*, vol. 117, no. 778, pp. 610–624, 1928.
- [24] S. Murakami, “Phase transition between the quantum spin hall and insulator phases in 3d: Emergence of a topological gapless phase,” *New Journal of Physics*, vol. 9, no. 9, p. 356, 2007.
- [25] L. Fu, C. L. Kane, and E. J. Mele, “Topological insulators in three dimensions,” *Physical review letters*, vol. 98, no. 10, p. 106 803, 2007.

- [26] H. Guo and S.-Q. Shen, “Topological phase in a one-dimensional interacting fermion system,” *Physical Review B*, vol. 84, no. 19, p. 195 107, 2011.
- [27] J. K. Asbóth, L. Oroszlány, and A. Pályi, “A short course on topological insulators,” *Lecture notes in physics*, vol. 919, pp. 997–1000, 2016.
- [28] M. V. Berry, “Quantal phase factors accompanying adiabatic changes,” *Proceedings of the Royal Society of London. A. Mathematical and Physical Sciences*, vol. 392, no. 1802, pp. 45–57, 1984.
- [29] M. Kohmoto, “Topological invariant and the quantization of the hall conductance,” *Annals of Physics*, vol. 160, no. 2, pp. 343–354, 1985.
- [30] J. Avron, L. Sadun, J. Segert, and B. Simon, “Topological invariants in fermi systems with time-reversal invariance,” *Physical review letters*, vol. 61, no. 12, p. 1329, 1988.
- [31] M. Stone and P. Goldbart, *Mathematics for physics: a guided tour for graduate students*. Cambridge University Press, 2009.
- [32] L. Fu and C. L. Kane, “Time reversal polarization and a z_2 adiabatic spin pump,” *Physical Review B*, vol. 74, no. 19, p. 195 312, 2006.
- [33] T. Fukui and Y. Hatsugai, “Quantum spin hall effect in three dimensional materials: Lattice computation of z_2 topological invariants and its application to bi and sb,” *Journal of the Physical Society of Japan*, vol. 76, no. 5, pp. 053 702–053 702, 2007.
- [34] J. E. Moore and L. Balents, “Topological invariants of time-reversal-invariant band structures,” *Physical Review B*, vol. 75, no. 12, p. 121 306, 2007.
- [35] M. Z. Hasan and C. L. Kane, “Colloquium: Topological insulators,” *Reviews of modern physics*, vol. 82, no. 4, p. 3045, 2010.
- [36] X.-L. Qi and S.-C. Zhang, “Topological insulators and superconductors,” *Reviews of Modern Physics*, vol. 83, no. 4, p. 1057, 2011.
- [37] T. Yokoyama, A. V. Balatsky, and N. Nagaosa, “Gate-controlled one-dimensional channel on the surface of a 3d topological insulator,” *Physical review letters*, vol. 104, no. 24, p. 246 806, 2010.
- [38] R. Seshadri and D. Sen, “Confining dirac electrons on a topological insulator surface using potentials and a magnetic field,” *Physical Review B*, vol. 89, no. 23, p. 235 415, 2014.

- [39] Z. Alpichshev, J. Analytis, J.-H. Chu, I. Fisher, and A. Kapitulnik, “Stm imaging of a bound state along a step on the surface of the topological insulator Bi_2Te_3 ,” *Physical Review B*, vol. 84, no. 4, p. 041 104, 2011.
- [40] N. Fedotov and S. Zaitsev-Zotov, “Experimental search for one-dimensional edge states at surface steps of the topological insulator Bi_2Se_3 : Distinguishing between effects and artifacts,” *Physical Review B*, vol. 95, no. 15, p. 155 403, 2017.
- [41] Y. Xu, G. Jiang, J. Chiu, L. Miao, E. Kotta, Y. Zhang, R. R. Biswas, and L. A. Wray, “Connection topology of step edge state bands at the surface of a three dimensional topological insulator,” *New Journal of Physics*, vol. 20, no. 7, p. 073 014, 2018.
- [42] A. C. Neto, F. Guinea, N. M. Peres, K. S. Novoselov, and A. K. Geim, “The electronic properties of graphene,” *Reviews of modern physics*, vol. 81, no. 1, p. 109, 2009.
- [43] T. Wehling, A. M. Black-Schaffer, and A. V. Balatsky, “Dirac materials,” *Advances in Physics*, vol. 63, no. 1, pp. 1–76, 2014.
- [44] L. Tarruell, D. Greif, T. Uehlinger, G. Jotzu, and T. Esslinger, “Creating, moving and merging dirac points with a fermi gas in a tunable honeycomb lattice,” *Nature*, vol. 483, no. 7389, pp. 302–305, 2012.
- [45] M. Bellec, U. Kuhl, G. Montambaux, and F. Mortessagne, “Topological transition of dirac points in a microwave experiment,” *Physical review letters*, vol. 110, no. 3, p. 033 902, 2013.
- [46] H.-Z. Lu, W.-Y. Shan, W. Yao, Q. Niu, and S.-Q. Shen, “Massive dirac fermions and spin physics in an ultrathin film of topological insulator,” *Physical review B*, vol. 81, no. 11, p. 115 407, 2010.
- [47] Y. Xu, G. Jiang, I. Miotkowski, R. R. Biswas, and Y. P. Chen, “Tuning insulator-semimetal transitions in 3d topological insulator thin films by intersurface hybridization and in-plane magnetic fields,” *Physical review letters*, vol. 123, no. 20, p. 207 701, 2019.
- [48] A. Zyuzin, M. Hook, and A. a. Burkov, “Parallel magnetic field driven quantum phase transition in a thin topological insulator film,” *Physical Review B*, vol. 83, no. 24, p. 245 428, 2011.
- [49] F. Klinkhamer and G. Volovik, “Emergent cpt violation from the splitting of fermi points,” *International Journal of Modern Physics A*, vol. 20, no. 13, pp. 2795–2812, 2005.

- [50] C. Lin, X. He, J. Liao, X. Wang, V. Sacksteder IV, W. Yang, T. Guan, Q. Zhang, L. Gu, G. Zhang, *et al.*, “Parallel field magnetoresistance in topological insulator thin films,” *Physical Review B*, vol. 88, no. 4, p. 041 307, 2013.
- [51] J. Liao, Y. Ou, X. Feng, S. Yang, C. Lin, W. Yang, K. Wu, K. He, X. Ma, Q.-K. Xue, *et al.*, “Observation of anderson localization in ultrathin films of three-dimensional topological insulators,” *Physical review letters*, vol. 114, no. 21, p. 216 601, 2015.
- [52] Q. Niu, D. J. Thouless, and Y.-S. Wu, “Quantized hall conductance as a topological invariant,” *Physical Review B*, vol. 31, no. 6, p. 3372, 1985.
- [53] X.-g. Wen and A. Zee, “Shift and spin vector: New topological quantum numbers for the hall fluids,” *Physical review letters*, vol. 69, no. 6, p. 953, 1992.
- [54] R. R. Biswas and D. T. Son, “Fractional charge and inter-landau-level states at points of singular curvature,” *Proceedings of the National Academy of Sciences*, vol. 113, no. 31, pp. 8636–8641, 2016.
- [55] J. C. Slater and G. F. Koster, “Simplified leao method for the periodic potential problem,” *Physical Review*, vol. 94, no. 6, p. 1498, 1954.
- [56] A.-L. He, W.-W. Luo, Y.-F. Wang, and C.-D. Gong, “Chern insulators in singular geometries,” *Physical Review B*, vol. 97, no. 4, p. 045 126, 2018.
- [57] A. Rüegg and C. Lin, “Bound states of conical singularities in graphene-based topological insulators,” *Physical review letters*, vol. 110, no. 4, p. 046 401, 2013.
- [58] T. Li, P. Zhu, W. A. Benalcazar, and T. L. Hughes, “Fractional disclination charge in two-dimensional c n-symmetric topological crystalline insulators,” *Physical Review B*, vol. 101, no. 11, p. 115 115, 2020.
- [59] R. Tamura, K. Akagi, M. Tsukada, S. Itoh, and S. Ihara, “Electronic properties of polygonal defects in graphitic carbon sheets,” *Physical Review B*, vol. 56, no. 3, p. 1404, 1997.
- [60] A. P. Schnyder, S. Ryu, A. Furusaki, and A. W. Ludwig, “Classification of topological insulators and superconductors in three spatial dimensions,” *Physical Review B*, vol. 78, no. 19, p. 195 125, 2008.
- [61] A. Kitaev, “Periodic table for topological insulators and superconductors,” in *AIP conference proceedings*, American Institute of Physics, vol. 1134, 2009, pp. 22–30.
- [62] J. Avron, R. Seiler, and P. G. Zograf, “Viscosity of quantum hall fluids,” *Physical review letters*, vol. 75, no. 4, p. 697, 1995.

- [63] N. Read, “Non-abelian adiabatic statistics and hall viscosity in quantum hall states and p x+ i p y paired superfluids,” *Physical Review B*, vol. 79, no. 4, p. 045 308, 2009.
- [64] C. Hoyos and D. T. Son, “Hall viscosity and electromagnetic response,” *Physical review letters*, vol. 108, no. 6, p. 066 805, 2012.
- [65] Y. Chen, G. Jiang, and R. R. Biswas, “Geometric response of quantum hall states to electric fields,” *Physical Review B*, vol. 103, no. 15, p. 155 303, 2021.
- [66] M. Johnson and B. Lippmann, “Motion in a constant magnetic field,” *Physical Review*, vol. 76, no. 6, p. 828, 1949.
- [67] D. Yoshioka, *The quantum Hall effect*. Springer Science & Business Media, 2013, vol. 133.
- [68] J. E. Moyal, “Quantum mechanics as a statistical theory,” in *Mathematical Proceedings of the Cambridge Philosophical Society*, Cambridge University Press, vol. 45, 1949, pp. 99–124.
- [69] E. Abbena, S. Salamon, and A. Gray, *Modern differential geometry of curves and surfaces with Mathematica*. CRC press, 2017.
- [70] D. R. Hofstadter, “Energy levels and wave functions of bloch electrons in rational and irrational magnetic fields,” *Physical review B*, vol. 14, no. 6, p. 2239, 1976.
- [71] R. Peierls, “Zur theorie des diamagnetismus von leitungselektronen,” *Zeitschrift für Physik*, vol. 80, no. 11-12, pp. 763–791, 1933.
- [72] Y. Hatsugai, “Topological aspects of the quantum hall effect,” *Journal of Physics: Condensed Matter*, vol. 9, no. 12, p. 2507, 1997.
- [73] J. Zak, “Magnetic translation group,” *Physical Review*, vol. 134, no. 6A, A1602, 1964.
- [74] E. Brown, “Bloch electrons in a uniform magnetic field,” *Physical Review*, vol. 133, no. 4A, A1038, 1964.
- [75] Y. Chen and R. R. Biswas, “Gauge-invariant variables reveal the quantum geometry of fractional quantum hall states,” *Physical Review B*, vol. 102, no. 16, p. 165 313, 2020.

A. ANALYTICAL SOLUTION TO BOUNDARY STATES OF MODIFIED DIRAC EQUATIONS

In reference [20], [22], perturbation method was used to solve the modified Dirac equations (MDE) for boundary states in two and three-dimensional space. Here I provide exact solutions of MDE in one, two and three-dimensional space.

A.1 One-Dimensional Space

The eigenvector associated with energy E of Hamiltonian (1.13) when p_x is replaced with $-i\lambda$ is

$$\chi = \begin{pmatrix} i\lambda \\ m + B\lambda^2 - E \end{pmatrix}, \quad (\text{A.1})$$

where E is related to λ through Equation (1.14). For the bound state to vanish at $x = 0$, it is required $\chi_1 = \chi_2$, i.e.

$$\frac{i\lambda_1}{m + B\lambda_1^2 - E} = \frac{i\lambda_2}{m + B\lambda_2^2 - E}, \quad (\text{A.2})$$

where $\lambda_{1,2}$ are two roots with negative real parts sorted out based on condition (1.17). One notices the sorting result depends on sign of $1 + 4B^2E^2 - 4mB$ only.

For the case $1 + 4B^2E^2 - 4mB < 0$, no matter $mB > \frac{1}{2}$ or $< \frac{1}{2}$, the two roots with negative real part are

$$\begin{aligned} \lambda_1 &= -\sqrt{\frac{1}{2B^2}(1 - 2mB + \sqrt{1 - 4mB + 4B^2E^2})}, \\ \lambda_2 &= \sqrt{\frac{1}{2B^2}(1 - 2mB - \sqrt{1 - 4mB + 4B^2E^2})}. \end{aligned} \quad (\text{A.3})$$

Plug into Equation (A.2) one obtains the possible solutions $E = 0, m$ and $\pm \frac{\sqrt{-1+4mB}}{2B}$, where the latter three are eliminated by condition $1 + 4B^2E^2 - 4mB < 0$.

For the other case $1 + 4B^2E^2 - 4mB > 0$, the two roots with negative real part are

$$\begin{aligned}\lambda_1 &= -\sqrt{\frac{1}{2B^2}(1 - 2mB + \sqrt{1 - 4mB + 4B^2E^2})}, \\ \lambda_2 &= -\sqrt{\frac{1}{2B^2}(1 - 2mB - \sqrt{1 - 4mB + 4B^2E^2})}.\end{aligned}\tag{A.4}$$

One can get the same four solutions of E and again the latter three are eliminated. In this case since both $\lambda_{1,2}$ are negative, from (A.2) one notices $\lambda_1\lambda_2 = m/B$ is positive, so $mB > 0$.

To conclude, when topological condition $mB > 0$ is satisfied, the only boundary state has energy $E = 0$.

A.2 Two-Dimensional Space

When p_x, p_y are replaced with $-i\lambda, k_y$ respectively, the eigenvector associated with energy E of Hamiltonian (1.19) is

$$\chi = \begin{pmatrix} i(\lambda + k_y) \\ m + B\lambda^2 - Bk_y^2 - E \end{pmatrix},\tag{A.5}$$

where E is related to λ through Equation (1.20). For the bound state to vanish at $x = 0$, it is required

$$\frac{i(\lambda_1 + k_y)}{m + B\lambda_1^2 - Bk_y^2 - E} = \frac{i(\lambda_2 + k_y)}{m + B\lambda_2^2 - Bk_y^2 - E},\tag{A.6}$$

where $\lambda_{1,2}$ are two roots with negative real parts sorted out based on condition (1.22).

For the case $1 + 4B^2E^2 - 4mB < 0$, the two roots with negative real part are

$$\begin{aligned}\lambda_1 &= -\sqrt{\frac{1}{2B^2}(1 - 2mB + 2B^2k_y^2 + \sqrt{1 + 4B^2E^2 - 4mB})}, \\ \lambda_2 &= \sqrt{\frac{1}{2B^2}(1 - 2mB + 2B^2k_y^2 - \sqrt{1 + 4B^2E^2 - 4mB})}.\end{aligned}\tag{A.7}$$

Plug into Equation (A.6) one obtains the possible solutions $E = \pm k_y, m$ and $\pm \frac{\sqrt{-1+4mB}}{2B}$, where the latter three are eliminated by condition $1 + 4B^2E^2 - 4mB < 0$. To determine $E = k_y$ or $-k_y$, notice in this case $\lambda_{1,2}$ have been simplified to

$$\lambda_{1,2} = -\frac{1}{2|B|}(1 \pm \sqrt{1 - 4mB + 4B^2k_y^2}). \quad (\text{A.8})$$

Plug into (A.6) one obtains the final solution $E = \text{sgn}(B)k_y$.

For the other case $1 + 4B^2E^2 - 4mB > 0$, the two roots with negative real part are

$$\begin{aligned} \lambda_1 &= -\sqrt{\frac{1}{2B^2}(1 - 2mB + 2B^2k_y^2 + \sqrt{1 + 4B^2E^2 - 4mB})}, \\ \lambda_2 &= -\sqrt{\frac{1}{2B^2}(1 - 2mB + 2B^2k_y^2 - \sqrt{1 + 4B^2E^2 - 4mB})}. \end{aligned} \quad (\text{A.9})$$

Similarly one can get $E = \pm k_y$, therefore $\lambda_{1,2}$ are simplified to

$$\begin{aligned} \lambda_1 &= -\frac{1}{2|B|}(1 + \sqrt{1 - 4mB + 4B^2k_y^2}), \\ \lambda_2 &= -\frac{1}{2|B|}|1 - \sqrt{1 - 4mB + 4B^2k_y^2}|. \end{aligned} \quad (\text{A.10})$$

By plugging into (A.6) one can find to have a solution, λ_2 must be equal to $-(1/2|B|)(1 - \sqrt{1 - 4mB + 4B^2k_y^2})$, which imposes constraints $mB > 0$ and $|E| < \sqrt{m/B}$. The energy spectrum is still $E = \text{sgn}(B)k_y$.

To conclude, when topological condition $mB > 0$ is satisfied, the edge states exist with spectrum $E = \text{sgn}(B)k_y$ and limited in the range $|E| < \sqrt{m/B}$.

A.3 Three-Dimensional Space

When p_x, p_y, p_z are replaced with $-i\lambda, k_y, k_z$ respectively, the two eigenvectors associated with energy E of Hamiltonian (1.24) are

$$\begin{aligned}\chi_1 &= \begin{pmatrix} \frac{ik_y + \lambda}{k_y^2 + k_z^2 - \lambda^2} (Bk_y^2 + Bk_z^2 - m - B\lambda^2 - E) \\ \frac{k_z}{k_y^2 + k_z^2 - \lambda^2} (Bk_y^2 + Bk_z^2 - m - B\lambda^2 - E) \\ 0 \\ 1 \end{pmatrix}, \\ \chi_2 &= \begin{pmatrix} \frac{-k_z}{k_y^2 + k_z^2 - \lambda^2} (Bk_y^2 + Bk_z^2 - m - B\lambda^2 - E) \\ \frac{i(\lambda - k_y)}{k_y^2 + k_z^2 - \lambda^2} (Bk_y^2 + Bk_z^2 - m - B\lambda^2 - E) \\ 1 \\ 0 \end{pmatrix}\end{aligned}\tag{A.11}$$

where E is related to λ through Equation (1.25). For the bound state to vanish at $x = 0$, it is required

$$a_1\chi_1(\lambda_1) + b_1\chi_2(\lambda_1) = a_2\chi_1(\lambda_2) + b_2\chi_2(\lambda_2),\tag{A.12}$$

where $\lambda_{1,2}$ are two roots with negative real parts sorted out based on the decaying condition

$$\begin{aligned}1 + 4B^2E^2 - 4mB &< 0, \\ \text{or, } 1 + 4B^2E^2 - 4mB &> 0 \text{ and } mB < \frac{1}{2} + B^2(k_y^2 + k_z^2) \\ \text{and } E^2 &< (k_y^2 + k_z^2) + (m - Bk_y^2 - Bk_z^2)^2.\end{aligned}\tag{A.13}$$

Inspecting Equation (A.12), one must have $a_1 = a_2$, $b_1 = b_2$. Then (A.12) leads to a determinant equation

$$\det [\tilde{\chi}_1(\lambda_1) - \tilde{\chi}_1(\lambda_2), \tilde{\chi}_2(\lambda_1) - \tilde{\chi}_2(\lambda_2)] = 0,\tag{A.14}$$

where $\tilde{\chi}_i$ is a two-dimensional vector formed by the first two components of χ_i .

For the case $1 + 4B^2E^2 - 4mB < 0$, the two roots with negative real part are

$$\begin{aligned}\lambda_1 &= -\sqrt{\frac{1}{2B^2}[1 - 2mB + 2B^2(k_y^2 + k_z^2) + \sqrt{1 + 4B^2E^2 - 4mB}]}, \\ \lambda_2 &= \sqrt{\frac{1}{2B^2}[1 - 2mB + 2B^2(k_y^2 + k_z^2) - \sqrt{1 + 4B^2E^2 - 4mB}]}. \end{aligned} \quad (\text{A.15})$$

Plug into Equation (A.14) one obtains the possible solutions $E = \pm\sqrt{k_y^2 + k_z^2}$ and $-m$, where $E = -m$ is eliminated by $1 + 4B^2E^2 - 4mB < 0$. In this case, $\lambda_{1,2}$ are simplified to

$$\lambda_{1,2} = -\frac{1}{2|B|}[1 \pm \sqrt{1 - 4mB + 4B^2(k_y^2 + k_z^2)}] \quad (\text{A.16})$$

For the other case $1 + 4B^2E^2 - 4mB > 0$, the two roots with negative real part are

$$\begin{aligned}\lambda_1 &= -\sqrt{\frac{1}{2B^2}[1 - 2mB + 2B^2(k_y^2 + k_z^2) + \sqrt{1 + 4B^2E^2 - 4mB}]}, \\ \lambda_2 &= -\sqrt{\frac{1}{2B^2}[1 - 2mB + 2B^2(k_y^2 + k_z^2) - \sqrt{1 + 4B^2E^2 - 4mB}]}. \end{aligned} \quad (\text{A.17})$$

Similarly one can get the dispersion $E = \pm\sqrt{k_y^2 + k_z^2}$, and $\lambda_{1,2}$ are simplified to

$$\begin{aligned}\lambda_1 &= -\frac{1}{2|B|}[1 + \sqrt{1 - 4mB + 4B^2(k_y^2 + k_z^2)}], \\ \lambda_2 &= -\frac{1}{2|B|}[1 - \sqrt{1 - 4mB + 4B^2(k_y^2 + k_z^2)}]. \end{aligned} \quad (\text{A.18})$$

By plugging into (A.12) one can find a solution exists only when $\lambda_2 = -(1/2|B|)[1 - \sqrt{1 - 4mB + 4B^2(k_y^2 + k_z^2)}]$, which imposes constraints $mB > 0$ and $|E| < \sqrt{m/B}$.

To conclude, when topological condition $mB > 0$ is satisfied, the surface states exist with spectrum $E = \pm\sqrt{k_y^2 + k_z^2}$ and limited in the range $|E| < \sqrt{m/B}$.

B. GAUGE TRANSFORMATION TO JOIN THE DISCLINATION

B.1 Unitary Representation of the Rotation Symmetry

I am using the convention that R and U correspond to fundamental counterclockwise rotation of a lattice model. For an m -sector disclination, the sectors are labeled by w which goes from 1 to m counterclockwise. R acts on real space vectors while the operator acting on quantum states is denoted by \hat{R} (with a hat).

For a flat lattice Hamiltonian

$$\hat{\mathcal{H}}_0 = \sum_{\mathbf{r}\delta} \hat{\Psi}_{\mathbf{r}+\delta}^\dagger t(\delta) \hat{\Psi}_{\mathbf{r}}, \quad (\text{B.1})$$

the rotational invariance

$$t(R\delta) = U t(\delta) U^{-1} \quad (\text{B.2})$$

implies that U matrix furnishes a unitary representation for the rotation symmetry of Hamiltonian. In other words, if one defines the action \hat{R} on states as

$$\hat{R}|\mathbf{r}, \alpha\rangle = U_{\beta\alpha} |R\mathbf{r}, \beta\rangle, \quad \langle \mathbf{r}, \alpha | \hat{R}^\dagger = U_{\beta\alpha}^* \langle R\mathbf{r}, \beta |, \quad (\text{B.3})$$

where \mathbf{r} is the vector label of unit cells and α, β are indices for internal degrees of freedom, then easy to check $\hat{\mathcal{H}}_0$ and \hat{R} commute

$$\hat{R} \hat{\mathcal{H}}_0 \hat{R}^{-1} = \hat{\mathcal{H}}_0. \quad (\text{B.4})$$

B.2 Join the Boundary

There are two ways of labeling orbital basis states on a flat lattice with some deficiency angle (the flat lattice has been divided into m sectors but not joined into disclination yet). One way is $|\mathbf{r}, \alpha\rangle$ as used in Equation (B.3), where \mathbf{r} can go to any unit cell on the entire flat

lattice. The other way is $|w, \mathbf{r}, \alpha\rangle$ which includes label of sectors, but then \mathbf{r} will be positions restricted in sector 1 only. The two notations are related by

$$|w, \mathbf{r}, \alpha\rangle = |R^{w-1}\mathbf{r}, \alpha\rangle \quad (\text{B.5})$$

with \mathbf{r} restricted in sector 1 again. Since the first labeling way will be no longer suitable for disclinations, the Hamiltonian language will be translated to second way. The matrix elements of flat lattice Hamiltonian now become

$$\langle w, \mathbf{r}, \alpha | \hat{\mathcal{H}}_0 | w, \mathbf{r}, \beta \rangle = t(R^{w-1}\mathbf{r} - R^{w-1}\mathbf{r})_{\alpha\beta}. \quad (\text{B.6})$$

In order to join the seam of flat lattice to make a disclination, a disclination Hamiltonian $\hat{\mathcal{H}}$ needs to be defined. In particular, one needs to define the hopping elements from sector m to sector 1 across the seam. To do this, I perform a gauge transformation at the edge of sector 1, i.e. define new orbital basis

$$\widetilde{|1, \mathbf{r}, \alpha\rangle}_{\text{edge}} \equiv |1, \mathbf{r}, \beta\rangle_{\text{edge}} (U^{-m})_{\beta\alpha} \quad (\text{B.7})$$

where the summation over dummy indices is suppressed. After this transformation the hoppings along edge of sector 1 become

$$\text{edge} \langle \widetilde{1, \mathbf{r}, \alpha} | \hat{\mathcal{H}}_0 | \widetilde{1, \mathbf{r}, \beta} \rangle_{\text{edge}} = (U^{-m})_{\delta\alpha}^* \text{edge} \langle 1, \mathbf{r}, \delta | \hat{\mathcal{H}}_0 | 1, \mathbf{r}, \gamma \rangle_{\text{edge}} (U^{-m})_{\gamma\beta} = t(R^m\mathbf{r} - R^m\mathbf{r})_{\alpha\beta}. \quad (\text{B.8})$$

Equation (B.8) says the new hoppings along edge of sector 1 are equal to these along edge of sector m in their local frame, therefore the bonds across seam can be naturally defined as same as these in sector m but perpendicular to the edge. The definition is

$$\text{edge} \langle \widetilde{1, \mathbf{r}, \alpha} | \hat{\mathcal{H}} | m, \mathbf{r}, \beta \rangle_{\text{edge}} \equiv t(R^m\mathbf{r} - R^{m-1}\mathbf{r})_{\alpha\beta}. \quad (\text{B.9})$$

Also after transformation (B.7), the hoppings in sector 1 from edge to sites near the edge but without being transformed will undergo some adaptive change. The new matrix elements are

$$\langle 1, \mathbf{r}, \alpha | \hat{\mathcal{H}}_0 | \widetilde{1, \mathbf{r}, \beta} \rangle_{\text{edge}} = \langle 1, \mathbf{r}, \alpha | \hat{\mathcal{H}}_0 | 1, \mathbf{r}, \gamma \rangle_{\text{edge}} (U^{-m})_{\gamma\beta} = [t(\mathbf{r} - \mathbf{r}') U^{-m}]_{\alpha\beta}. \quad (\text{B.10})$$

Equation (B.8), (B.9) and (B.10) complete the definition of disclination Hamiltonian $\hat{\mathcal{H}}$.

C. A PERIODIC DEFINITION OF THE DISCLINATION HAMILTONIAN

One can perform an additional gauge transformation on the disclination Hamiltonian $\hat{\mathcal{H}}$ defined in Appendix C, making the hoppings periodic in each sector. In this definition, the seam between sector m and 1 looks exactly same as other nodal lines between neighboring sectors, therefore proving the disclination Hamiltonian $\hat{\mathcal{H}}$ is everywhere locally flat except at disclination center.

This additional gauge transformation is defined as

$$|w, \mathbf{r}, \alpha\rangle^p \equiv |w, \mathbf{r}, \beta\rangle (U^{w-1})_{\beta\alpha}, \quad (\text{C.1})$$

where the superscript p means under this basis the disclination Hamiltonian $\hat{\mathcal{H}}$ will be periodic. Special attention should be paid to the orbital basis at edge of sector 1. Combining (B.7), it means

$$|1, \mathbf{r}, \alpha\rangle_{\text{edge}}^p = \widetilde{|1, \mathbf{r}, \beta\rangle_{\text{edge}}} (U^m)_{\beta\alpha}. \quad (\text{C.2})$$

After transformation (C.1), the hoppings within sector w become

$${}^p\langle w, \mathbf{r}, \alpha | \hat{\mathcal{H}}_0 | w, \mathbf{r}, \beta \rangle^p = t(\mathbf{r} - \mathbf{r})_{\alpha\beta}, \quad 1 \leq w \leq m, \quad (\text{C.3})$$

where both \mathbf{r}, \mathbf{r} are restricted in sector 1 so they are independent of w . The hoppings across nodal lines between neighboring sectors become

$${}^p\langle w+1, \mathbf{r}, \alpha | \hat{\mathcal{H}}_0 | w, \mathbf{r}, \beta \rangle^p = [U^{-1}t(R\mathbf{r} - \mathbf{r})]_{\alpha\beta}, \quad 1 \leq w \leq m-1, \quad (\text{C.4})$$

which are also independent of w . The final step is to examine the hoppings from sector m to 1 across the seam. They are

$${}_{\text{edge}}{}^p\langle 1, \mathbf{r}, \alpha | \hat{\mathcal{H}} | m, \mathbf{r}, \beta \rangle_{\text{edge}}^p = (U^m)_{\gamma\alpha}^* {}_{\text{edge}}\langle \widetilde{1, \mathbf{r}, \gamma} | \hat{\mathcal{H}} | m, \mathbf{r}, \delta \rangle_{\text{edge}} (U^{m-1})_{\delta\beta} = [U^{-1}t(R\mathbf{r} - \mathbf{r})]_{\alpha\beta} \quad (\text{C.5})$$

which is the same as (C.4). Equations (C.3), (C.4) and (C.5) complete the proof of periodicity of disclination Hamiltonian $\hat{\mathcal{H}}$ under basis $|w, \mathbf{r}, \alpha\rangle^p$.